AUT Journal of Modeling and Simulation

AUT J. Model. Simul., 56(2) (2024) 129-154
DOI: 10.22060/miscj.2024.22932.5350

Numerical Algorithm for Simulation of Hybrid-Degrees of Freedom Belt-Pulley Systems: Application to X-Y Positioning Mechanism

M. M. Ebrahimi, M. R. Homaeinezhad *

Faculty of Mechanical Engineering, K. N. Toosi University of Technology, Tehran, Iran

ABSTRACT: This paper presents a comprehensive investigation into the modeling and dynamic analysis of a XY mechanism, considering the potential occurrence of motor pulley slipping. The research commenced with the establishment of kinematic relationships among system components and the definition of virtual pulleys. By characterizing static and kinetic frictions for individual system elements, various rolling and slipping states were explored. The study unveiled that the system, excluding motor pulleys, experiences a stick-slip phenomenon due to friction between actuator components and the ground, resulting in deadzones during motion initiation. To address this, a novel friction model encompassing deadzones was introduced, and equations accounting for the stick-slip phenomenon were derived. Moreover, recognizing that each actuator motor can be in either a rolling or slipping state, it was established that the mechanism represents a hybrid-DOF dynamic system. The equations of motion switch between four modes, denoted as RR, SR, RS, and SS, contingent on input voltages, kinematic and dynamic variables, and friction coefficients between motor pulleys and belts. Calculating the required friction to maintain rolling was essential; insufficient friction between motor pulleys and belts leads to motor slipping. The determination of the system's subsequent dynamics considered different motor states, varying DOF, and the interplay of stick-slip phenomena with deadzones. Ultimately, dynamic analyses of the mechanism were conducted through simulations in three distinct scenarios. This study effectively highlights the nonlinear effects and complexities inherent in this mechanism, offering valuable insights into its behavior under different conditions.

Review History:

Received: Jan. 16, 2024
Revised: Dec. 01, 2024
Accepted: Dec. 02, 2024
Available Online: Dec. 19, 2024

Keywords:

Hybrid Degrees of Freedom
Nonlinear Mechanics
Stick-Slip Phenomenon
Hybrid Deadzone
Coulomb (Dry) Friction

1- Introduction

1- 1- Overview

The XY mechanism has emerged as a pivotal innovation in the realm of mechanical systems and precision engineering, offering unparalleled precision and accuracy. Its synchronized belt arrangement minimizes backlash and positional errors, resulting in finer and more detailed prints and cuts. This mechanism's efficiency is evident in its rapid and smooth movement, achieved through coordinated motor control and parallel belt paths, which reduce production times and enhance CNC machining operations. Moreover, the CoreXY design's emphasis on reduced inertia facilitates quicker acceleration and deceleration, ultimately translating into faster overall speeds. This harmonious movement also mitigates vibrations and sudden shifts, ensuring consistent layer heights in 3D printing and achieving precise cuts in CNC machining. The versatility of the CoreXY mechanism finds application in a wide array of industries that demand exacting movement control. In the realm of 3D printing, it facilitates the creation of intricate designs, reduces vibrations for improved layer adhesion, and expedites the production of detailed prints. CNC machining benefits from its precision, enabling intricate tasks such as milling, engraving, and cutting. Industries engaged in prototyping and rapid manufacturing capitalize on CoreXY's accuracy for crafting functional prototypes and small-scale production runs. From high-technology industries, where intricate components meet stringent quality benchmarks, to the healthcare sector, which requires precision in medical devices, CoreXY mechanisms offer reliable performance. Despite its transformative potential, the mathematical modeling of the CoreXY mechanism presents a set of intricate challenges. Its complex kinematic structure gives rise to nonlinear relationships between motor inputs and positional outcomes, necessitating meticulous derivation of accurate mathematical expressions. Cross-axis coupling introduces further complexity, requiring the consideration of interactions between the x and y axes for precise modeling. Ensuring proper synchronization of belts and accounting for their behavior, along with belt stretch and tension, is paramount for an accurate model. Incorporating motor

*Corresponding author's email: mrhomaeinezhad@kntu.ac.ir

dynamics, friction, wear, and discretization into the model demands a comprehensive understanding of mechanical and dynamic behavior.

Frictional elements, including pulleys, are intrinsic to the CoreXY mechanism and significantly influence its dynamic behavior. Friction, aside from opposing the system's motion, necessitates an increase in actuator energy, and due to its inherently unpredictable behavior, introduces nonlinearity into the system's dynamics. One notable nonlinearity arising from the transition in frictional states is the stick-slip phenomenon, wherein the continuous change in forces and torques between static and kinetic states leads to highly intricate and nonlinear system behavior. The CoreXY mechanism comprises several movable components, each potentially in either a static or kinetic state, depending on the mechanism's kinematics. Hence, it is imperative to consider the stick-slip phenomenon comprehensively for all components within the mechanism based on kinematic relationships. Another undesirable effect of friction is the creation of a deadzone when the system initiates motion [1]. In other words, when an object is at rest with static friction against a surface, an input force must be applied sufficiently to overcome static friction and set it in motion, resulting in the confinement of the system's dynamic input to a deadzone function [2]. Another nonlinear factor contributing to the complexity of the CoreXY mechanism's dynamics is the possibility of pulley slippage in actuator motors. Depending on the instantaneous speed and acceleration of the system's components, applying voltage inputs to the actuator motors may cause individual motor pulleys to transition between rolling and slipping states or vice versa. Moreover, pulley slippage effectively separates the motor from the system's dynamics, granting it independent motion, and consequently increasing the system's DOF. Therefore, by accounting for the possibility of slippage in each motor, the CoreXY mechanism may exhibit 2, 3, or 4 DOF, with transitions occurring between them at any given moment. As a result, the CoreXY mechanism does not conform to a unified dynamic model and behaves as a hybrid-DOF system. In this paper, considering various rolling/slipping states for the two actuator motors, the dynamic modeling of the mechanism has been undertaken, presenting a switchable model encompassing four distinct states.

1- 2- Literature Review

The domain of mechanical systems and precision engineering has witnessed a resurgence, sparked by a succession of groundbreaking inquiries, each embarking on a unique voyage to unravel the complexities of frictional adjustment, dynamic governance, and advanced motion mechanisms. Through methodical explorations and inventive methodologies, these investigations have made substantial contributions to the progression of mechanical design and positioning technologies, expanding the horizons of performance, precision, and productivity. One particularly noteworthy exploration venture into the realm of frictional adaptation, a crucial pursuit in the quest for enhanced accuracy and control [3], [4]where deep learning (DL. In the study [5], researchers delved into the subtleties of friction dynamics within a planar slider, employing parameter estimation methods to formulate a comprehensive friction model [6]. This model was subsequently incorporated into a PID controller, resulting in the attainment of flawless positional tracking accuracy, thereby providing invaluable insights into the dynamic attenuation of frictional forces. Within the expansive domain of additive manufacturing, the study [7]additive manufacturing has grown steadily and found numerous applications across all types of industries. More recently, the industry has seen a spur of growth as the terms of the original patents expired and new companies entered the market. While there exist several different methods of additive manufacturing, polymer-based material extrusion 3D printing (also known as fused filament fabrication introduces a groundbreaking endeavor centered around a large-scale 3D printing device. This innovation harnesses the geometry of a different shape, maximizing its advantages through the application of simplified kinematic equations. Not only does this approach enhance printing accuracy, but it also establishes the groundwork for efficient large-scale printing processes. The pursuit of dynamic control and precision takes the spotlight in the study [8], where the concept of adaptive fuzzy-logic deadzone compensation plays a pivotal role. This study delves into the intricacies of positioning control for an XY table, introducing advanced control strategies that effectively mitigate deadzone effects through adaptive control algorithms [9]. This approach exemplifies the harmonious interaction between dynamic control and compensation, providing a holistic solution for improved motion precision. Building upon the distinctive framework of this new mechanism, study [10] embarks on a comprehensive exploration of kinematic and dynamic modeling. Employing Lagrange equations, the study meticulously dissects dynamic behaviors. Notably, the consideration of friction, now in a new light, enriches the understanding of the intricate dynamics of the system. Study [11] resonates with the desire for linear and seamless motion by unveiling a groundbreaking mechanism with characteristics that minimize backward and nonlinear motion properties. Through ingenious engineering, this innovative mechanism achieves a linear and continuous motion trajectory. Additionally, the incorporation of a flexure mechanism further enhances motion continuity, with friction serving as a critical non-switching element within the dynamic equations. Amidst this vibrant landscape, study [12] presents an exploration into a hollow-type piezoelectric positioning platform, introducing a three-stage flexible lever amplification. This innovative platform design offers a novel approach to motion amplification, carefully considering flexible mechanisms and piezoelectric properties. In doing so, this study contributes a layer of complexity and adaptability to motion systems within the field of precision engineering. Furthermore, study [13] sheds light on the intricacies of modeling robotic systems with closed-circuit belt-pulley transmissions. The study reveals the complexities of belt-pulley network friction, encompassing factors such as

belt tension, pulley wrap angles, and the number of pulleys [14]. Employing multi-friction models for pulleys, the research navigates the multifaceted interplay of frictional forces, further expanding the realm of dynamic modeling. In numerous mechanical systems involving contact between surfaces, the challenge of friction poses significant design complexities for control systems. Frictional forces manifest between surfaces in both static and kinetic forms, characterized by their inherently nonlinear nature, which defies precise mathematical modeling [15], [16]. Additionally, the transition from static to kinetic friction, as well as the point at which movement commences or ceases, remains obscure. Given the inherent uncertainties introduced by friction in control systems, numerous researchers have approached the problem by treating friction as a disturbance during controller design and employing estimators, such as state observers, to approximate its effects. In a noteworthy instance, in 1989, Ostertag and colleagues devised an observer tailored to estimate the dry friction effects exerted on an inverted pendulum system. This innovative approach enabled the system's control through state feedback mechanisms [17], [18], [19]. In reality, the constant transformation between static and kinetic friction ushers in a perpetual cycle of motion and halts, a phenomenon often termed as stick-slip [20], [21]. This occurrence can wield detrimental consequences on the control of systems where surface interaction prevails. Employing a switching model and integrating feedback control, particularly in scenarios involving dry friction such as brake systems, servo systems contending with friction, vibration-propelled locomotion systems, ultrasonic motors, drilling apparatus, haptic devices characterized by friction, and the dynamic dynamics of seismic fault lines, emerges as a viable approach to govern systems susceptible to the stick-slip phenomenon [22], [23]. To illustrate, within the realm of oil and gas drilling, the stick-slip phenomenon constitutes a pivotal consideration [24]. Given the unpredictable environmental conditions surrounding the drilling process and the nonlinearity of frictional forces, the behavior of the drilling equipment inherently adopts nonlinear characteristics. When delving into friction modeling, it becomes imperative to effectively capture the system's switching dynamics [25]. The Stribeck model emerges as one of the most prevalent models employed in systems grappling with friction, offering insights into friction as a function of motion velocity [26], [27]. On the flip side, within mechanical systems, the frictional resistance to motion, whether in static or kinetic states, incurs energy losses and escalates the power demands placed on the actuator for system control. In situations where the system is at rest, any applied actuator force must surpass the static friction force's magnitude for motion to initiate. Consequently, within the range where the actuator force remains inferior to the static friction force, the system encounters a deadzone. This deadzone can manifest with either symmetric upper and lower boundaries [28] or asymmetric boundaries [29].

1- 3- Contributions and Innovations

Based on the conducted literature review, the innovative contributions in this paper can be organized as follows:

- Novel Friction Model: The paper introduces a new friction model that incorporates deadzones, addressing the limitations of traditional friction models which do not account for these phenomena.
- Stick-Slip Analysis: It explores the stick-slip phenomenon specifically in the context of the XY mechanism, highlighting how friction between actuator components and the ground results in motion deadzones.
- Hybrid DOF Dynamic System: The research establishes the mechanism as a hybrid degrees of freedom (DOF) dynamic system, recognizing that each actuator motor can be in different states (rolling or slipping).
- Dynamic Equations of Motion: The paper derives equations of motion that switch between four distinct operational modes (RR, SR, RS, SS), depending on various factors such as input voltages and friction coefficients.
- Comprehensive State Analysis: It provides a detailed analysis of the system dynamics based on different motor states and their impact on motion, which includes assessing the required friction to maintain rolling to prevent slipping.
- Simulations for Dynamic Analysis: Finally, the study includes dynamic analyses conducted through simulations across three different scenarios, effectively demonstrating the nonlinear behaviors of the mechanism under varied conditions.

The remaining sections of this paper are organized as follows. Section 2 covers an explanation of the CoreXY mechanism's operation, the actuators used to set it in motion, the derivation of kinematic relationships within the system, the establishment of dynamic equations for the central mechanism, a description of the introduced model for stick-slip with deadzones, the procedure for detecting friction sign changes, the hybrid-DOF dynamic modeling, and the method for identifying system rolling/slipping states as a precursor for further steps. Section 3 involves the simulation of the derived equations using MATLAB and the dynamic analysis of the mechanism with its inherent nonlinearities. Section 4 will conclude the findings presented in this paper.

Fig. 1 illustrates the flowchart of the hybrid-DOF system modeling algorithm presented in this paper. As shown in Fig. 1, the process begins by using the kinematic data of the manipulator to calculate the velocities and accelerations of the driven pulleys and virtual pulleys, which are then used to determine whether the system is in a rolling or slipping state. Additionally, the motor dynamics and the friction between the belt and the motor pulleys are considered to compute the input torque for the Hybrid Dynamics Equations.

Based on the rolling or slipping state in the previous time step (k-1), the state of the system in the current time step (k) is identified and applied as a trigger to the switching dynamic

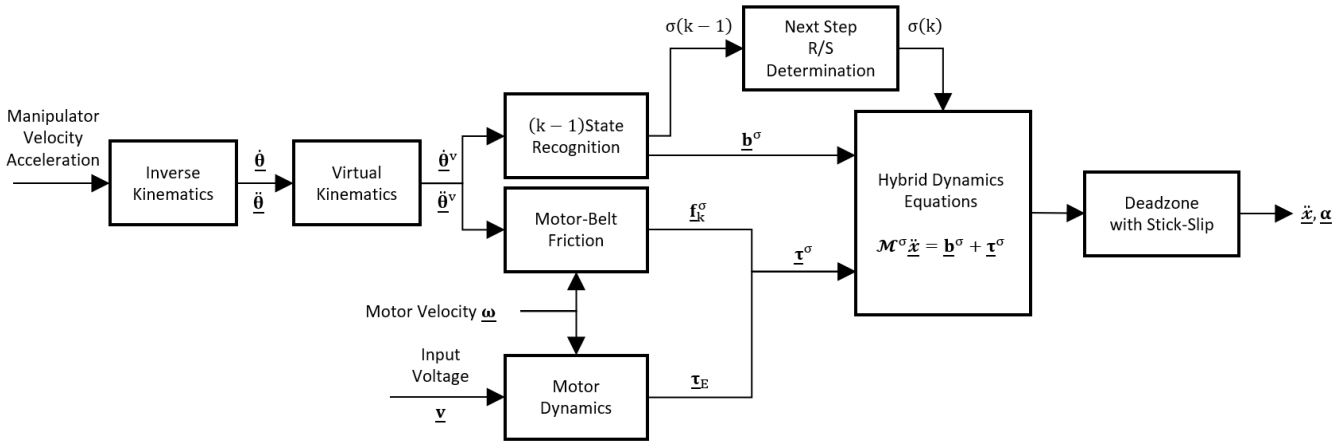

Fig. 1. Flowchart of the dynamic modeling algorithm for the hybrid-DOF system

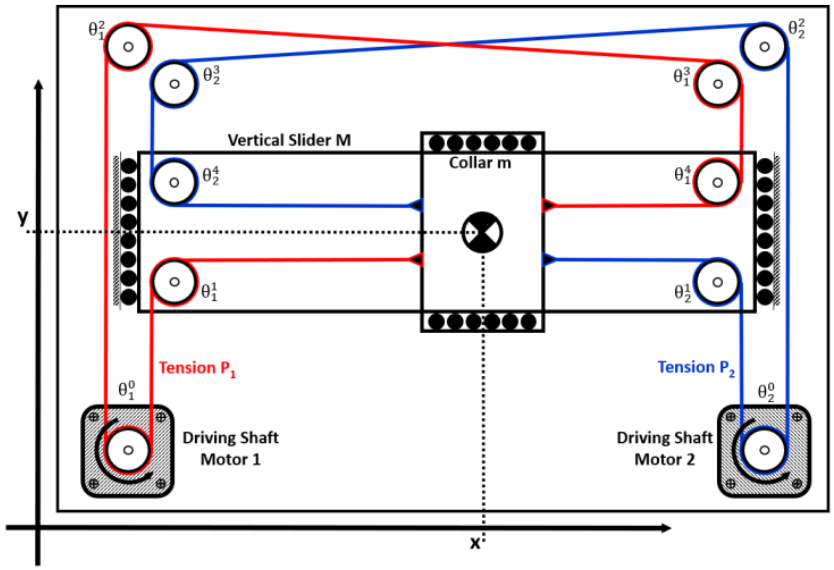

Fig. 2. An overhead view of the CoreXY mechanism, comprising DC servo motors, torque-transmitting pulleys, and two sliders on horizontal and vertical rails. The system is configured as a hybrid-DOF dynamic system which can have 2, 3 or 4 DOF in the different rolling/slipping modes, with the use of two belts with different initial tensions.

equations. Finally, the output accelerations of the manipulator and the motors are calculated, taking into account the effects of deadzone and the stick-slip phenomenon.

2- XY Mechanism Example Introduction

In this section, the CoreXY mechanism is initially explained as an example of belt-pulley mechanisms. As depicted in Fig. 2, the CoreXY mechanism utilizes two DC servo motors along with 8 pulleys to actuate a collar with mass m on a vertical slider with mass M. This system is a 2-DOF mechanism, and by appropriately adjusting the voltages applied to the two motors as the system inputs, the position of the collar can be controlled in the XY plane. Furthermore, to transmit the generated torques from the motors to the sliders, two belts with tensions P_1 and P_2 are employed.

To name the pulleys, angle symbols are employed as indicated in Fig. 2. Subscript 1 is used for the pulleys connected to Belt 1, and subscript 2 is assigned to pulleys connected to Belt 2. Subsequently, after examining the equations related to the system's actuators, the kinematics and dynamics of the mechanism will be derived, considering the modeling assumptions described below.

Assumptions

- The belts, labeled as Belt 1 and Belt 2, have constant initial tensions, represented by P_1 and P_2.
- Neglecting the effects of weight, friction, and the nonlinear behavior of belt motion, the belts maintain a constant length during movement and do not undergo any bending.
- The mechanism's pulleys may come into contact with dry friction against the ground and can either be stationary or in motion.
- All pulleys, except for the motor-driven ones, are always in a rolling state and do not slip.
- The interaction between the motor pulleys and the belts can involve either rolling or slipping, corresponding to static or kinetic friction, respectively.

2- 1- Assumed Servo Actuators

As observed in Fig. 2, two DC servo motors have been employed to actuate the mechanism. By applying voltage inputs to each of the motors, the output torque of these motors can be adjusted. Subsequently, the equations pertaining to the system's actuators are extracted in accordance with Eqs. (1)-(3).

$$\tau^{E} = K_t i \tag{1}$$

$$i = -\frac{K_e}{R}\omega + \frac{1}{R}v \tag{2}$$

$$\tau^{E} = -\frac{K_t K_e}{R}\omega + \frac{K_t}{R}v \tag{3}$$

As depicted in Eq. (1), the output torque of the DC motor τ^{E}, is proportional to the current intensity i, multiplied by a constant coefficient K_t. On the other hand, in accordance with Eq. (2), the current intensity generated in the DC motor increases with an increase in input voltage v, and the rotational speed of the motor is affected by the multiplication of the voltage effects by the back EMF coefficient K_e. Therefore, by substituting Eq. (2) into Eq. (1), the output torque of the motor can be calculated as a function of the input voltage and the rotational speed of the motor. In these equations, R represents the resistance of the motor's armature winding.

2- 2- CoreXY Collar-Belt Kinematics

In this section, considering the DOF x and y for the system, the kinematics of the CoreXY mechanism, including the rotational velocities and accelerations of the pulleys, are derived. As illustrated in Fig. 2, 8 pulleys are employed to transmit the torques from the motors to the sliders. The relationships for their velocities can be expressed in terms of $\dot{x}$ and $\dot{y}$ as shown in Eqs. (4)-(11). Additionally, by taking derivatives of the velocity equations, the pulley accelerations can also be readily obtained in terms of x and y, which will have similar relationships to the velocity equations.

$$\dot{\theta}_1^1 = -\frac{\dot{x}}{r} \tag{4}$$

$$\dot{\theta}_1^2 = \frac{\dot{x} + \dot{y}}{r} \tag{5}$$

$$\dot{\theta}_1^3 = \frac{\dot{x} + \dot{y}}{r} \tag{6}$$

$$\dot{\theta}_1^4 = \frac{\dot{x}}{r} \tag{7}$$

$$\dot{\theta}_2^1 = -\frac{\dot{x}}{r} \tag{8}$$

$$\dot{\theta}_2^2 = \frac{\dot{x} - \dot{y}}{r} \tag{9}$$

$$\dot{\theta}_2^3 = \frac{\dot{x} - \dot{y}}{r} \tag{10}$$

$$\dot{\theta}_2^4 = \frac{\dot{x}}{r} \tag{11}$$

Where r represents the radius of the pulleys, and it is assumed that all pulleys, including the motor pulleys, have the same uniform radius and $\dot{\theta}_j^i$, demonstrates the angular velocity of the i^{th} pully driven by j^{th} motor.

2- 3- Belt-Connected Virtual Pulleys

In this section, two virtual pulleys are introduced in the region where the motors are located, and it is assumed that the motion of these pulleys occurs smoothly along with the mechanism without any slippage. This allows us to divide the entire system into three parts: motor 1 on the left, motor 2 on the right, and the central 2-DOF mechanism, referred to as the "central mechanism." Therefore, the velocities and accelerations of the virtual pulleys, which are part of the central mechanism, can be expressed in terms of the velocities and accelerations of the DOF as shown in Eqs. (12)-(15).

$$\dot{\theta}_1^v = \frac{\dot{x} + \dot{y}}{r} \tag{12}$$

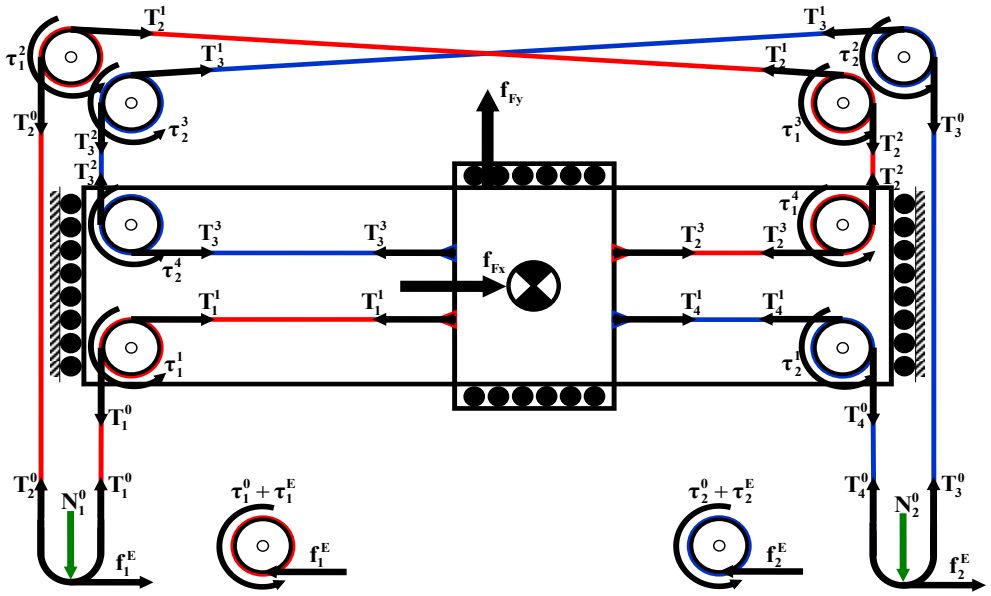

Fig. 3. Free-body diagram of CoreXY system components, including tension forces, torques, and friction forces between the ground and system components, friction forces between belts and motor pulleys

$$\dot{\theta}_2^v = \frac{\dot{x} - \dot{y}}{r} \tag{13}$$

$$\ddot{\theta}_1^v = \frac{\ddot{x} + \ddot{y}}{r} \tag{14}$$

$$\ddot{\theta}_2^v = \frac{\ddot{x} - \ddot{y}}{r} \tag{15}$$

2- 4- Dynamic Modelling of Hybrid DOF System

In this section, considering the internal forces and torques acting on the components of the system, at first the dynamic equations for the central mechanism are derived. Then, the different hybrid dynamic states of the system are examined. As depicted in Fig. 3, the tensile forces acting on each of the system's components, including the pulleys and sliders, denoted as T, along with the torques and friction forces, represented by τ and f, respectively, are specified.

Remark 1. As illustrated in Fig. 3, for each of the pulleys, two tension forces are depicted with identical subscripts. When the belt passes over each pulley, due to the pulley's torque or its rotational inertia, a difference in tension forces on both sides of the pulley is created, denoted as ΔP. Prior to motion, the tension forces on both sides of the pulley are equal and equivalent to the initial tension force, P. Assuming the transfer of the same amount of tension force from one side to the other side of the pulley, it is possible to consider the sum of the tension forces before and after motion as $2P$.

In Fig. 3, the motor pulleys are separated from the system, and the forces and torques acting on each component are illustrated. Applying voltage inputs to each of the motors, torque τ_1^E and τ_2^E are generated in motors 1 and 2, respectively. Friction torques between the motor pulleys and the ground are denoted as τ_1^0 and τ_2^0, respectively. Due to the contact between motor pulleys and the belts, contact forces f_1^E and f_2^E are transmitted to motors 1 and 2, which are of static or kinetic friction, and these forces depend on the interaction of the pulleys with the belts. Moreover, vertical forces on the surface, adjusted to the tension in the belts and the weight of the sliders, are taken into account. Since the belts wrap around the motor pulleys 180 degrees, the vertical force between the belt and each motor pulley (with $i = 1, 2$ corresponding to each belt) is calculated as $2P_i$. However, for the 8 passive pulleys used in the central mechanism, considering an approximate 90-degree angle for the belt around each pulley, the vertical force between the belt and each passive pulley is considered as $\sqrt{2}P_i$. Additionally, the vertical forces acting on the horizontal and vertical rails are proportional to the weight on the rails and can be calculated as $N_x = mg$ and $N_y = (M+m)g$, respectively.

2- 4- 1- Dynamic Equations of Collar-Belt System

Taking into consideration the forces and torques depicted in Fig. 3, the dynamic equations for the central mechanism can be written as Eqs. (16)-(25).

$$+T_1^0 r - T_1^1 r + \tau_1^1 = J' \frac{-\ddot{x}}{r} \quad (16)$$

$$+T_4^1 r - T_4^0 r + \tau_2^1 = J' \frac{-\ddot{x}}{r} \quad (17)$$

$$+T_2^0 r - T_2^1 r + \tau_1^2 = J' \frac{\ddot{x} + \ddot{y}}{r} \quad (18)$$

$$+T_3^1 r - T_3^0 r + \tau_2^2 = J' \frac{\ddot{x} - \ddot{y}}{r} \quad (19)$$

$$+T_2^1 r - T_2^2 r + \tau_1^3 = J' \frac{\ddot{x} + \ddot{y}}{r} \quad (20)$$

$$+T_3^2 r - T_3^1 r + \tau_2^3 = J' \frac{\ddot{x} - \ddot{y}}{r} \quad (21)$$

$$+T_2^2 r - T_2^3 r + \tau_1^4 = J' \frac{+\ddot{x}}{r} \quad (22)$$

$$+T_3^3 r - T_3^2 r + \tau_2^4 = J' \frac{+\ddot{x}}{r} \quad (23)$$

$$+T_2^3 r + T_4^1 r - T_3^3 r - T_1^1 r + f_x r = mr\ddot{x} \quad (24)$$

$$+T_2^2 r + T_3^2 r - T_1^0 r - T_4^0 r + f_y r = (M + m)r\ddot{y} \quad (25)$$

where J' represents the inertia of the pulleys, f_x denotes the frictional force on the horizontal rail, and f_y represents the frictional force on the vertical rail.

2- 4- 2- Friction States and Direction Detection

The force or torque resulting from friction differs between a static object and a moving one. When a force or torque is applied to a static object, static friction is generated in the opposite direction of the applied force or torque. The static friction continues to build up until the magnitude of the applied force or torque exceeds the static friction, at which point the object will start accelerating, denoted as $\mathcal{A}$. Since static friction opposes the initiation of motion, its direction is determined by the direction of acceleration, and the magnitude of the frictional force or torque can be calculated using Eq. (26). After the initiation of motion and the application of acceleration, the object's velocity reaches a non-zero value, represented as ϑ. At this point, the direction of kinetic friction is opposite to the direction of the object's velocity. The kinetic friction can be calculated using Eq. (27).

$$f_s = -N\mu_s \text{sign}(\mathcal{A}) \quad (26)$$

$$f_k = -N\mu_k \text{sign}(v) \quad (27)$$

In these equations, N represents the normal force, μ_s is the coefficient of static friction, μ_k is the coefficient of kinetic friction, f_s stands for static friction, and f_k represents kinetic friction, which are applied to the object.

2- 4- 3- Stick-Slip with Deadzone Function Definition

It is assumed that the dynamic system with unit inertia is subjected to friction f, which can take on values f_s and f_k in two states: static friction and kinetic friction. The acceleration of this system is calculated according to Eq. (28), where f_E and f_f denote the representative terms of external forces (torques) and friction forces, respectively. When f_E is applied to the dynamic system, its behavior can be described as a function $\mathcal{F}(f_E, f_s, f_k, \vartheta)$, as shown in Eq. (29). Additionally, the deadzone function, denoted by DZ, which represents the deadzone at the start of motion, can be obtained using Eq. (30).

$$\ddot{x} = f_E + f_f \quad (28)$$

$$\ddot{x} = \mathcal{F}(f_E, f_s, f_k, v) = \begin{cases} DZ(f_E, f_s, v = 0) & v = 0 \\ f_E + f_k & v \neq 0 \end{cases} \quad (29)$$

$$DZ(f_E, f_s, v = 0) = \begin{cases} 0 & |f_E| < |f_s| \\ f_E + f_s & \text{else} \end{cases} \quad (30)$$

In other words, a dynamic system can exhibit two states: static and kinetic. In the first state, static friction prevents motion, while in the second state, kinetic friction hinders the system's motion. When an external force is applied to the system while it is at rest, two scenarios may occur, determined by the deadzone function. If the magnitude of the external force is insufficient to overcome static friction, the system's acceleration is calculated as zero. However, if the external force can overcome static friction, the system's acceleration is calculated as the sum of the applied force and the static friction, resulting in a non-zero acceleration. In the kinetic state, when the body has a non-zero velocity, kinetic friction is constantly applied constant with a value of f_k and

in the direction opposite to the body's velocity.

2- 4- 4- Motor-Belt Friction Definition

Taking into account the friction between the belt and the pulley of each motor in both static and kinetic states, the friction force can be considered as shown in Eqs. (31)-(34). As can be seen, the direction of kinetic friction depends on the velocity difference between the motor pulley and the virtual pulley, while static friction's direction is determined by the difference in acceleration between the motor pulley and the virtual pulley. The magnitude of kinetic friction can be taken as a constant, assuming a constant coefficient of kinetic friction. However, determining the magnitude of static friction is not possible independently and is equal to the motor torque applied to the pulley until it reaches its maximum value, at which point it turns into kinetic friction. The maximum static friction can be determined using Eq. (33)-(34). In these equations, the sign of the acceleration of the motor pulley as well as the virtual pulley depends on the applied motor torques.

$$f_{1k}^{b} = -2\mu_{1k}^{b} P_1 \mathrm{sgn}\left(\omega_1 - \dot{\theta}_1^{v}\right) \tag{31}$$

$$f_{2k}^{b} = -2\mu_{2k}^{b} P_2 \mathrm{sgn}\left(\omega_2 - \dot{\theta}_2^{v}\right) \tag{32}$$

$$f_{1smax}^{b} = -2\mu_{1smax}^{b} P_1 \mathrm{sgn}\left(\alpha_1 - \ddot{\theta}_1^{v}\right) \tag{33}$$

$$f_{2smax}^{b} = -2\mu_{2smax}^{b} P_2 \mathrm{sgn}\left(\alpha_2 - \ddot{\theta}_2^{v}\right) \tag{34}$$

In which μ_{1k}^{b} and μ_{2k}^{b} are the coefficients of kinetic friction between the pulleys and the motor belts number 1 and 2. Also, the speed and acceleration of motor number 1 are denoted by ω_1 and α_1, and the speed and acceleration of motor number 2 are represented by ω_2 and α_2.

Remark 2. Since the contact between the motor pulley and the belt depends on their relative speed and acceleration, it is necessary to use the relative speed and acceleration when calculating the static and kinetic friction between the pulley and the belt. These relative speed and acceleration values are determined based on the motion of the motor pulley as well as the speed and acceleration of the virtual pulley, which is essentially connected to the belt.

2- 4- 5- Rolling/Slipping Hybrid-DOF Dynamic Equations

With the dynamic system presented in Fig. 3, dynamic equations can be considered for different scenarios in which the left and right motors are either in a rolling or slipping state. Thus, four modes can be defined for the system, each governed by different dynamic equations. The general equation governing the dynamics of the central mechanism can be formulated as Eq. (35), where $\mathcal{M}^{\acute{o}}$ represents the inertia matrix, $\underline{\mathbf{b}}^{\sigma}$ is a vector containing the frictions of the pulleys and sliders, and $\underline{\tau}^{\sigma}$ is the vector of forces and torques acting on the central mechanism.

$$\mathcal{M}^{\sigma}\underline{\ddot{x}} = \underline{\mathbf{b}}^{\sigma} + \underline{\boldsymbol{\tau}}^{\sigma} \tag{35}$$

Remark 3. The dynamic system of the CoreXY mechanism, assuming the two motors can be in a rolling or slipping state, is a hybrid switching system. This is due to the fact that if each of the motors is in a rolling state, their motion is effectively coupled with the central mechanism, following its DOF. However, if a motor is in a slipping state, its motion becomes independent of the central mechanism and adds one degree of freedom to the system. As a result, the dynamic system can have either 2, 3, or 4 DOF at any given moment. Moreover, a unique identifier will be assigned to each dynamic mode, denoted as DMN_i (Dynamic Model Number), where i can take values from 1 to 4.

I . RR: Motor 1 and Motor 2 Rolling: 2 DOF, $\mathbf{DMN}_1$

In the first scenario, both motors are assumed to be in a rolling state, and the system functions as a unified 2-DOF mechanism. In this configuration, the system's DOF is defined as the positions along the x and y axes. All angles, including those of the pulleys and motors, can be expressed in terms of these coordinates. Assuming a rolling state for both motors, the dynamic equation for each motor can be represented as Eqs. (36)-(37).

$$+T_1^0 r - T_2^0 r + \tau_1^0 + \tau_1^E = J\frac{\ddot{x} + \ddot{y}}{r} \tag{36}$$

$$+T_3^0 r - T_4^0 r + \tau_2^0 + \tau_2^E = J\frac{\ddot{x} - \ddot{y}}{r} \tag{37}$$

Thus, by considering these two equations along with the equations derived in Section 2.4.1, the dynamic equations governing the system can be formulated as Eq. (35), where the matrix. $\mathcal{M}^{I}$ and the two vectors $\underline{\mathbf{b}}^{I}$ and $\underline{\tau}^{I}$ are calculated using Eqs. (38)-(40).

$$\mathcal{M}^{I} = \begin{bmatrix} mr + \dfrac{8J'}{r} + \dfrac{2J}{r} & 0 \\ 0 & (M+m)r + \dfrac{4J'}{r} + \dfrac{2J}{r} \end{bmatrix} \tag{38}$$

$$\underline{\mathbf{b}}^{I} = \begin{bmatrix} +\tau_1^0 + \tau_1^1 + \tau_1^2 + \tau_1^3 + \tau_1^4 + \tau_2^0 + \tau_2^1 + \tau_2^2 + \tau_2^3 + \tau_2^4 + f_x r \\ +\tau_1^0 + \tau_1^2 + \tau_1^3 - \tau_2^0 - \tau_2^2 - \tau_2^3 + f_y r \end{bmatrix} \tag{39}$$

$$\underline{\boldsymbol{\tau}}^{\mathrm{I}} = \begin{bmatrix} \tau_1^{\mathrm{E}} + \tau_2^{\mathrm{E}} \\ \tau_1^{\mathrm{E}} - \tau_2^{\mathrm{E}} \end{bmatrix} \tag{40}$$

Additionally, in this scenario, as both motors are in a rolling state, their angular acceleration and velocity can be expressed in terms of the DOF of the middle mechanism, as shown in Eqs. (41)-(44).

$$\alpha_1 = \ddot{\theta}_1^{\mathrm{v}} = \frac{\ddot{x} + \ddot{y}}{r} \tag{41}$$

$$\alpha_2 = \ddot{\theta}_2^{\mathrm{v}} = \frac{\ddot{x} - \ddot{y}}{r} \tag{42}$$

$$\omega_1 = \dot{\theta}_1^{\mathrm{v}} = \frac{\dot{x} + \dot{y}}{r} \tag{43}$$

$$\omega_2 = \dot{\theta}_2^{\mathrm{v}} = \frac{\dot{x} - \dot{y}}{r} \tag{44}$$

II. SR: Motor 1 Slipping and Motor 2 Rolling: 3 DOF, $\mathbf{DMN}_2$

In this scenario, it is assumed that motor 1 is in a slipping state, while motor 2 is in a rolling state. As a result, with the independence of motor 1 due to slipping, one degree of freedom is added to the DOF of the mechanism, and the system will have three DOF. The equations related to the torques applied to the belts at the contact points with the motors can be seen in Eqs. (45),(46). Thus, the system consists of a 2-DOF mechanism on the right side of the system along with a motor on the left side of the system. As shown in Eq. (45), the frictional force between motor 1's pulley and the belt is transformed into a torque applied to the motor, denoted as $f_{1k}^{b} r$, and its reaction on the right-side mechanism.

$$+T_1^0 r - T_2^0 r + f_{1k}^{b} r = 0 \tag{45}$$

$$+T_3^0 r - T_4^0 r + \tau_2^0 + \tau_2^{\mathrm{E}} = J\frac{\ddot{x} - \ddot{y}}{r} \tag{46}$$

By eliminating the effects of the left-side motor from the equations and applying Eq. (46) to the equations of the central mechanism, the parameters of the dynamic equation Eq. (35) can be calculated as Eqs. (47)-(49).

$$\boldsymbol{\mathcal{M}}^{\mathrm{II}} = \begin{bmatrix} mr + \frac{8J'}{r} + \frac{J}{r} & -\frac{J}{r} \\ -\frac{J}{r} & (M+m)r + \frac{4J'}{r} + \frac{J}{r} \end{bmatrix} \tag{47}$$

By examining the inertia matrix presented in Eq. (47) and comparing it with the inertia matrix for the first rolling/slipping scenario presented in Eq. (38), it's evident that the inertia matrix in the second scenario is no longer diagonal, and the term $-\frac{J}{r}$ has appeared in the off-diagonal of the matrix. Consequently, it can be concluded that by disconnecting the left-side motor, the dynamic symmetry of the system has been disrupted, resulting in coupled dynamic equations.

$$\underline{\mathbf{b}}^{\mathrm{II}} = \begin{bmatrix} +\tau_1^1 + \tau_1^2 + \tau_1^3 + \tau_1^4 + \tau_2^0 + \tau_2^1 + \tau_2^2 + \tau_2^3 + \tau_2^4 + f_x r \\ +\tau_1^2 + \tau_1^3 - \tau_2^0 - \tau_2^2 - \tau_2^3 + f_y r \end{bmatrix} \tag{48}$$

$$\underline{\boldsymbol{\tau}}^{\mathrm{II}} = \begin{bmatrix} f_{1k}^{b} r + \tau_2^{\mathrm{E}} \\ f_{1k}^{b} r - \tau_2^{\mathrm{E}} \end{bmatrix} \tag{49}$$

The friction vector can be obtained using Eq. (48). As observed in Eq. (49), the torque vector for the right-side mechanism includes the torque resulting from the translational friction, which is $f_{1k}^{b} r$, acting as the actuator torque for the mechanism. Furthermore, the dynamic equation governing motor 1 can be formulated, considering the actuator torque $\tau_1^{\mathrm{E}} + f_{1k}^{b} r$ resulting from the translational friction between the motor's pulley and the belt, as presented in Eq. (50). Additionally, since motor 2 is in a rolling state, its acceleration and velocity need to be calculated using kinematic relations, and these are expressed as Eqs. (51),(53). Moreover, with the determination of the acceleration of motor 1, its angular velocity can be obtained by integrating the acceleration, as shown in Eq. (52).

$$J\alpha_1 = \tau_1^0 + \tau_1^{\mathrm{E}} + f_{1k}^{b} r \tag{50}$$

$$\alpha_2 = \ddot{\theta}_2^{\mathrm{v}} = \frac{\ddot{x} - \ddot{y}}{r} \tag{51}$$

$$\omega_1 = \int \alpha_1 \, dt \tag{52}$$

$$\omega_2 = \dot{\theta}_2^{\mathrm{v}} = \frac{\dot{x} - \dot{y}}{r} \tag{53}$$

III. RS: Motor 1 Rolling and Motor 2 Slipping: 3 DOF, $\mathbf{DMN}_3$

In this case, it is assumed that motor 1 is in a rolling state, while motor 2 is in a slipping state. Consequently, the system can be divided into two parts: motor 2 on the right and a 2-DOF mechanism on the left. The only connecting factor between them is the torque resulting from translational friction between the motor's pulley and the belt, denoted as $f_{2k}^{b}r$. Therefore, in this scenario, dynamic equations will be formulated for a 3-DOF system. The equations related to the belts at the points of contact with the motor's pulleys can be observed in Eqs. (54),(55).

$$+T_1^0 r - T_2^0 r + \tau_1^0 + \tau_1^E = J\frac{\ddot{x}+\ddot{y}}{r} \tag{54}$$

$$+T_3^0 r - T_4^0 r + f_{2k}^{b} r = 0 \tag{55}$$

As seen in Eq. (55), a torque of $f_{2k}^{b}r$ is applied to the belt due to the change in the state of motor 2 to slipping. In this scenario, by considering the equations of the middle mechanism, the parameters in Eq. (35) can be calculated as presented in Eqs. (56)-(58).

$$\boldsymbol{\mathcal{M}}^{III} = \begin{bmatrix} mr + \frac{8J'}{r} + \frac{J}{r} & \frac{J}{r} \\ \frac{J}{r} & (M+m)r + \frac{4J'}{r} + \frac{J}{r} \end{bmatrix} \tag{56}$$

$$\underline{\mathbf{b}}^{III} = \begin{bmatrix} +\tau_1^0 + \tau_1^1 + \tau_1^2 + \tau_1^3 + \tau_1^4 + \tau_2^1 + \tau_2^2 + \tau_2^3 + \tau_2^4 + f_x r \\ +\tau_1^0 + \tau_1^2 + \tau_1^3 - \tau_2^2 - \tau_2^3 + f_y r \end{bmatrix} \tag{57}$$

$$\underline{\boldsymbol{\tau}}^{III} = \begin{bmatrix} \tau_1^E + f_{2k}^{b} r \\ \tau_1^E - f_{2k}^{b} r \end{bmatrix} \tag{58}$$

As shown in Eq. (56), the inertia matrix is calculated in a non-diagonal form, indicating the loss of system dynamic symmetry due to the disconnection of motor 2, and the coupling of the dynamics of the mechanism on the left side. Furthermore, in Eq. (58), the torque resulting from the friction between the belt and motor 2 is applied to the mechanism on the left instead of τ_2^E. Next, the acceleration and velocity of motors 1 and 2 can be calculated as presented in Eqs. (59)-(62).

$$\alpha_1 = \ddot{\theta}_1^v = \frac{\ddot{x}+\ddot{y}}{r} \tag{59}$$

$$J\alpha_2 = \tau_2^0 + \tau_2^E + f_{2k}^E r \tag{60}$$

$$\omega_1 = \dot{\theta}_1^v = \frac{\dot{x}+\dot{y}}{r} \tag{61}$$

$$\omega_2 = \int \alpha_2 \, dt \tag{62}$$

Since motor 1 is in a rolling state, its acceleration and velocity are calculated based on virtual pulley 1, while for motor 2, its acceleration is determined based on the friction from the belt, and it defines the next step's angular velocity in integration.

IV. SS: Motor 1 and Motor 2 Slipping: 4 DOF, $\mathbf{DMN}_4$

The last scenario in which the dynamic system may exist is when both motors are in a slipping state. In this case, the dynamic system is divided into three subsystems, with two motors on the left and right sides and a 2-DOF mechanism in the center. Therefore, with both motors becoming independent, the dynamic system will act as a 4-DOF mechanism, and the torques resulting from the friction between the motors' pulleys and belts will be a factor in connecting the subsystems. The equations for the torques applied to the belts at the contact points with the motors can be written as Eqs. (63),(64).

$$+T_1^0 r - T_2^0 r + f_{1k}^{b} r = 0 \tag{63}$$

$$+T_3^0 r - T_4^0 r + f_{2k}^{b} r = 0 \tag{64}$$

By using Eqs. (63),(64) along with the equations for the dynamics of the central mechanism obtained in Section 2.4.1, the parameters of Eq. (35) can be calculated as shown in Eqs. (65)-(67).

$$\boldsymbol{\mathcal{M}}^{IV} = \begin{bmatrix} mr + \frac{8J'}{r} & 0 \\ 0 & (M+m)r + \frac{4J'}{r} \end{bmatrix} \tag{65}$$

As seen in Eq. (65), the inertia matrix in this case is similar to case I and is diagonal, indicating the symmetry of the system's dynamics and the decoupling of the slider motions from each other.

$$\underline{\mathbf{b}}^{IV} = \begin{bmatrix} +\tau_1^1 + \tau_1^2 + \tau_1^3 + \tau_1^4 + \tau_2^1 + \tau_2^2 + \tau_2^3 + \tau_2^4 + f_x r \\ +\tau_1^2 + \tau_1^3 - \tau_2^2 - \tau_2^3 + f_y r \end{bmatrix} \tag{66}$$

$$\underline{\boldsymbol{\tau}}^{\mathrm{IV}} = \begin{bmatrix} f_{1k}^{b} r + f_{2k}^{b} r \\ f_{1k}^{b} r - f_{2k}^{b} r \end{bmatrix} \tag{67}$$

In this case, considering that both motors are in a slipping state, the friction vector can be obtained using Eq. (66) and the actuation vector for the 2-DOF central mechanism will be as shown in Eq. (67), containing only the torques resulting from the friction between the pulleys of the motors and the belts. Accordingly, dynamic equations for each of the motors can also be written, taking into account the actuation torques $\tau_1^{E} + f_{1k}^{b} r$ for motor 1 and $\tau_2^{E} + f_{2k}^{b} r$ for motor 2 as shown in Eqs. (68),(69). Furthermore, angular velocities are calculated by integrating the accelerations according to Eqs. (70),(71).

$$J\alpha_1 = \tau_1^{0} + \tau_1^{E} + f_{1k}^{b} r \tag{68}$$

$$J\alpha_2 = \tau_2^{0} + \tau_2^{E} + f_{2k}^{b} r \tag{69}$$

$$\omega_1 = \int \alpha_1 \, dt \tag{70}$$

$$\omega_2 = \int \alpha_2 \, dt \tag{71}$$

2- 4- 6- Next Step Rolling/Slipping State Determination

As seen in Section 2.4.5, the dynamic equations of the system can have four different modes, in one of which, the system's degree of freedom and equation parameters are variable. To clarify the mode selection process, it is first determined which of the rolling/slipping states each motor is expected to be in after considering the system's kinematics at the current time $k-1$ and applying the input voltages to each of the motors, denoted as $v_1(k-1)$, $v_2(k-1)$. In order to discern the chosen mode, this process is initially performed for one of the motors. The dynamic system, consisting of the motor pulley and belt, can be in two states, denoted as $R(k-1)$ for rolling and $S(k-1)$ for slipping, where in both states, it can transition to $R(k)$ or $S(k)$ in the next time step k. According to Eq. (72), when the system is in $R(k-1)$, it is necessary to calculate the friction required to maintain the system in a rolling state, which corresponds to the static friction coefficient $\mu_s^{\star}(k)$. By comparing this friction coefficient with the actual static friction coefficient, it will be determined whether the system will continue rolling or if the available friction is insufficient, causing it to transition to slipping in the next time step.

$$R(k-1) \rightarrow \begin{cases} R(k): \mu_s^{b} \geq \mu_s^{\star}(k) \\ S(k): \mu_s^{b} < \mu_s^{\star}(k) \end{cases} \tag{72}$$

However, when the system, including the motor pulley and belt, is in the $S(k-1)$ state, as observed in Eq. (73), there is no static friction coefficient in play to determine the next state. Therefore, it is necessary to calculate the pulley motor and virtual pulley speeds in the next step. Then, it can be determined in which state the system is. If the speeds of the pulley motor and virtual pulley become equal in the next time step, indicating that their relative speed has become zero and the system has transitioned to a rolling state. However, if the speeds of the two pulleys are not equal, the system is still in a slipping state. Therefore, when the system is in $S(k-1)$, there is no need to determine the next state, and the kinematic variables, after integration, will specify the subsequent state of the system.

$$S(k-1) \rightarrow \begin{cases} R(k): \omega(k) = \dot{\theta}^{v}(k) \\ S(k): \omega(k) \neq \dot{\theta}^{v}(k) \end{cases} \tag{73}$$

In general, at time $k-1$, based on the mechanism's kinematics, the dynamic system can have four states: $RR(k-1)$, where both motors are in a rolling state; $SR(k-1)$, where motor 1 is slipping, and motor 2 is rolling; $RS(k-1)$, where motor 1 is rolling, motor 2 is slipping; and the last state $SS(k-1)$, where both motors are slipping. Similar to determining the state for one motor and belt, depending on the state of the mechanism at $k-1$, determining the state for both motors at k will be different. In this section, each of these states will be examined.

To calculate $\mu_s^{\star}(k)$, which represents the necessary friction coefficient to continue the rolling state, it is necessary to first calculate the ideal acceleration for the mechanism with the assumption of $R(k)$ for each state where the motor is in $R(k-1)$. This ideal acceleration is denoted as $\ddot{\underline{x}}^{\star}$ and is calculated using Eq. (74). This acceleration is, in fact, the ideal acceleration that the mechanism can achieve if no slipping occurs. Upon determining the ideal accelerations, the motor is separated from the mechanism, and its diagram is drawn. Taking into account the motor's acceleration from the kinematic equations, it is determined what friction force exists between the motor and the belt when the motor is in a rolling state. On the other hand, the maximum static friction force between the motor and the belt is also determined using the static friction coefficient. Therefore, $\mu_s^{\star}(k)$ and μ_s^{b} can be compared to determine whether the motor had enough friction or not, which will indicate the rolling or slipping state for the next step, respectively.

$$\mathcal{M}^{\sigma}\ddot{\underline{x}}(k-1)=\underline{b}^{\sigma}(k-1)+\underline{\tau}^{\sigma}(k-1);\quad \mathrm{DMN_i};\sigma=\mathrm{I,II,III,IV} \tag{74}$$

Remark 4. The ideal acceleration calculated using Eq. (74) signifies that a motor in a rolling state should remain in the same state in the subsequent step. Therefore, when calculating ideal accelerations, it is imperative to consider that $\mathrm{DMN_i}$ should also be chosen according to the corresponding ideal state.

Case $\mathbf{RR(k-1)}$

If the mechanism is in the $\mathrm{RR}(k-1)$ state, it is necessary to calculate the friction coefficients for each of the motors. These calculated coefficients should be compared with the real static friction coefficients of the system to determine whether the rolling/slipping state will persist in the next instant.

Remark 5. As observed in Section 2.4.5, the dynamic system has four different states with distinct dynamic equations. To calculate the required static friction coefficient for the continuation of the rolling state, dynamic system equations are used. Therefore, depending on the state the system is expected to be in the next step, the corresponding dynamic equations for that state should be utilized.

Assuming that the system is in $\mathrm{RR}(k-1)$, the ideal acceleration for the entire mechanism with both motors in the rolling state, represented by $\mathrm{DMN_1}$, is calculated. The ideal motor accelerations can be obtained using Eqs. (75),(76).

$$\hat{\alpha}_1=\frac{\ddot{x}+\ddot{y}}{r} \tag{75}$$

$$\hat{\alpha}_2=\frac{\ddot{x}-\ddot{y}}{r} \tag{76}$$

$$J\hat{\alpha}_1=\tau_1^0+\tau_1^E+f_{1s}^b r \tag{77}$$

$$J\hat{\alpha}_2=\tau_2^0+\tau_2^E+f_{2s}^b r \tag{78}$$

With the ideal accelerations of each motor determined, the dynamic equations for motor 1 and motor 2 will be as shown in Eqs. (77),(78). Using these equations, the static friction force required for rolling can be calculated as expressed in Eqs. (79),(80).

$$f_{1s}^b=J\frac{\ddot{x}+\ddot{y}}{r^2}-\frac{\tau_1^0+\tau_1^E}{r}= \mu_{1s}^{\star}2P_1\mathrm{sgn}\left[\alpha_1\left(f_1^b=0\right)-\ddot{\theta}_1^{v}\left(f_1^b=0\right)\right] \tag{79}$$

$$f_{2s}^b=J\frac{\ddot{x}-\ddot{y}}{r^2}-\frac{\tau_2^0+\tau_2^E}{r}= \mu_{2s}^{\star}2P_2\mathrm{sgn}\left[\alpha_2\left(f_2^b=0\right)-\ddot{\theta}_2^{v}\left(f_2^b=0\right)\right] \tag{80}$$

Where the sign of static friction is determined based on the angular acceleration of the motor relative to the virtual pulley when no friction is present. Thus, the coefficients $\mu_{1s}^{\star}$ and $\mu_{2s}^{\star}$, representing the static friction coefficients required to continue rolling, can be calculated as given in Eqs. (81),(82).

$$\mu_{1s}^{\star}=\frac{J}{2P_1}\left|\frac{\ddot{x}+\ddot{y}}{r^2}-\frac{\tau_1^0+\tau_1^E}{r}\right|;\mathrm{DMN_1} \tag{81}$$

$$\mu_{2s}^{\star}=\frac{J}{2P_2}\left|\frac{\ddot{x}-\ddot{y}}{r^2}-\frac{\tau_2^0+\tau_2^E}{r}\right|;\mathrm{DMN_1} \tag{82}$$

By determining the ideal static friction coefficients, the following scenarios can be examined for the system dynamics:

- RR **to** $RR(k):\mu_{1s}^{b}\geq\mu_{1s}^{\star}(k),\mu_{2s}^{b}\geq\mu_{2s}^{\star}(k);DMN_1$ In this case, the system will transition from $\mathrm{RR}(k-1)$ to $\mathrm{RR}(k)$. Therefore, it is necessary for the actual friction coefficients of the system for both motors to be sufficiently large to keep both motors in a rolling state. Moreover, since the system is expected to be in the $\mathrm{RR}(k)$ state, to calculate the required friction coefficients, the dynamic equation for motor 1, denoted as $\mathrm{DMN_1}$, should be utilized.
- RR **to** $SR(k):\mu_{1s}^{b}<\mu_{1s}^{\star}(k),\mu_{2s}^{b}\geq\mu_{2s}^{\star}(k);DMN_2$ In the second case, the friction for motor 1 is insufficient, and the system will transition to the $\mathrm{SR}(k)$ state. Therefore, it is necessary to use the equations of $\mathrm{DMN_2}$ for calculations.
- RR **to** $RS(k):\mu_{1s}^{b}\geq\mu_{1s}^{\star}(k),\mu_{2s}^{b}<\mu_{2s}^{\star}(k);DMN_3$ In the third case, the friction for motor 2 is insufficient, and the system will transition to the $\mathrm{RS}(k)$ state. Therefore, it is necessary to use the equations of $\mathrm{DMN_3}$ for calculations.
- RR **to** $SS(k):\mu_{1s}^{b}<\mu_{1s}^{\star}(k),\mu_{2s}^{b}<\mu_{2s}^{\star}(k);DMN_4$ In the final case, both motors will be in the slipping state, and the system will transition to $\mathrm{SS}(k)$. Therefore, it is necessary to use the equations of $\mathrm{DMN_4}$ for calculations.

Case $\mathbf{SR(k-1)}$

In this case, it is assumed that the system is in the $\mathrm{SR}(k-1)$ state. Therefore, it is only necessary to determine the state of motor 2, and this can be done by calculating $\mu_{2s}^{\star}(k)$ according to Eq. (83).

Table 1. Simulation parameters for the CoreXY mechanism along with values and descriptions

Parameter [Unit]	Value	Explanation	Parameter [Unit]	Value	Explanation
m [Kg]	0.5	Horizontal Collar Mass	μ_{1s}^{b}	Based on Scenario	Static Friction Coeff. Of Motor 1 With Belt
M [Kg]	1	Vertical Slider Mass	μ_{2s}^{b}	Based on Scenario	Static Friction Coeff. Of Motor 2 With Belt
J [Kg/m²]	0.001	Motors Pulley Inertial	f_{1k}^{b}	0.2	Kinetic Friction Coeff. Of Motor 1 With Belt
J′ [Kg/m²]	0.0005	Passive Pulleys Inertial	f_{2k}^{b}	0.2	Kinetic Friction Coeff. Of Motor 2 With Belt
r [m]	0.05	Pulleys Radius	ω_v [rad/s]	0.5	Input Voltage Frequency
R [Ω]	0.9	DC Motor Resistance	v_{01} [volts]	Based on Scenario	Motor 1 Voltage Amplitude
Kt [N.m/amp]	2	Motor Torque Constant	v_{02}[volts]	Based on Scenario	Motor 2 Voltage Amplitude
Ke [volt/rad /sec]	0.03	Electromotive Force Constant	P_1 [N]	Based on Scenario	Tension Force on Belt 1
μ_s	0.4	Static Friction Coeff. with Ground	P_2[N]	Based on Scenario	Tension Force on Belt 2
μ_k	0.1	Kinetic Friction Coeff. with Ground	T [sec]	0.0001	Simulation Time Step

$$\mu_{2s}^{\star} = \frac{J}{2P_2}\left|\frac{\ddot{x}-\ddot{y}}{r^2} - \frac{\tau_2^0+\tau_2^E}{r}\right|; DMN_2 \qquad (83)$$

- SR **to** $SR(k):\mu_{2s}^{b} \geq \mu_{2s}^{\star}(k); DMN_2$

In the first case, friction for motor 2 must be large enough to continue rolling. Since the $SR(k)$ the state is expected, it is necessary to use the equations DMN_2.

- SR **to** $SS(k):\mu_{2s}^{b} < \mu_{2s}^{\star}(k); DMN_4$

In the second case, friction for motor 2 is not sufficient, and motor 2 will be in a slipping state. Thus, the $SS(k)$ state will be applied to the system, and it is necessary to use the equations DMN_4.

Case $RS(k-1)$

In this case, it is assumed that the system is in the $RS(k-1)$ state. Therefore, it is only necessary to check the condition of motor 1's slipping. To do this, $\mu_{1s}^{\star}$ Can be calculated using.

$$\mu_{1s}^{\star} = \frac{J}{2P_1}\left|\frac{\ddot{x}+\ddot{y}}{r^2} - \frac{\tau_1^0+\tau_1^E}{r}\right|; DMN_3 \qquad (84)$$

- RS **to** $RS(k):\mu_{1s}^{b} \geq \mu_{1s}^{\star}(k); DMN_3$

In the first case, if the friction coefficient is sufficiently large, motor 1 will continue in its rolling state, and the system's dynamics will be of the DMN_3 mode.

- RS **to** $SS(k):\mu_{1s}^{b} < \mu_{1s}^{\star}(k); DMN_4$

In the second case, if the friction of motor 1 is not sufficiently large, it will transition into a slipping state. Therefore, the future state of the system will be $SS(k)$, and it is necessary to use the equations DMN_4 to calculate $\mu_{1s}^{\star}(k)$.

Case $SS(k-1)$

- **SS to $SS(k)$; DMN_4**

The last scenario occurs when both motors are in a slipping state. In this case, there is no need to determine the state for the next step, and the speeds of the pulleys in the next moment will dictate what the state will be.

3- Numerical Simulation and Discussions

In this section, in order to analyze the dynamic behavior of the presented model for the CoreXY mechanism while considering the dead zone caused by friction and the possibility of motor slipping, the system's outputs will be plotted for various motor voltage inputs. To achieve this, the dynamic equations will be numerically solved using MATLAB software, and the results will be presented. The parameters used in the simulation of the CoreXY mechanism are detailed in Table 1.

The information and parameters presented in Tables 1 and 2 are strategically curated to facilitate a comprehensive examination of all possible states of slipping, sliding, and deadzone behaviors within the XY mechanism across various scenarios. By employing a systematic approach to vary the defined parameters—such as friction coefficients, input

Table 2. Defined variable parameters for each simulation scenario, encompassing influential variables affecting the behavior of the CoreXY mechanism

Scenario #	Motor Input State	P_1, P_2 [N]	v_{01}, v_{02} [volts]	μ_{1s}^b, μ_{2s}^b
1	Harmonic	20, 20	10, 5	10, 0.1
2	Harmonic	30, 30	20, 10	0.001, 0.001
3	Piece − wise Step	20, 30	20, 10	10, 10

voltages, and kinematic variables—this study enables the generation of specific conditions under which each state can be initiated or exited. The scenarios are designed to reflect real-world operating conditions, allowing the mechanism to experience the full spectrum of dynamic behaviors, including the transition between stable rolling motion and the different slip states. Notably, the adjustments made to the system inputs are critical for manipulating the interplay between actuator dynamics and frictional forces. These manipulations effectively demonstrate how changes in voltage input or environmental conditions can lead to the onset of stick-slip phenomena or provoke the activation of deadzones during movement initiation. Furthermore, the data from Tables 1 and 2 serves as a baseline for computational simulations, which model how the mechanism responds to these input variations. By analyzing these results, the study not only reaffirms the presence of stick-slip behavior but also deepens our understanding of how varying input conditions influence the transition among rolling, slipping, and deadzone states. This holistic approach underscores the complexity of the system dynamics and highlights the importance of controlling the frictional interactions among the motor pulleys, belts, and actuator components.

Scenario 1:

Considering the parameters provided in Table 1 for simulating the CoreXY mechanism system, the input voltages for the actuator motors are generated as harmonic functions, given by $v_1 = v_{01}\sin(2\pi\omega_v t)$, $v_2 = v_{02}\cos(2\pi\omega_v t)$, where v_{01} and v_{02} are the voltage magnitudes, and ω_v is the frequency. The values of simulation parameters can be found in Table 2. In this scenario, the friction coefficient between motor 1 and the belt is significantly larger than the friction coefficient between motor 2 and the belt, making the chances of motor 1 slipping much lower compared to motor 2.

By applying the harmonic inputs defined in Scenario 1 to the system's governing equations, the resulting motion of the system and the motors is shown in Fig. 4. In Fig. 4-a, the acceleration, velocity, and position of each motor, along with the corresponding values for the virtual pulleys, are plotted. From this, it is evident that at certain moments, the velocity and acceleration of the motor pulley match those of the virtual pulley, indicating a rolling condition for the motor. In contrast, when the velocity and acceleration of the motor pulley and the virtual pulley differ, it signals a slipping condition for the motor. Initially, as depicted in Fig. 4-a, motor 1 remains in a rolling state, while motor 2 starts slipping right from the beginning. As the input voltage to the motors is increased, motor 1 also transitions into a slipping state. Fig. 4-b shows the motion of the central mechanism resulting from the calculated torques. Upon closer inspection of Fig. 4-b, it is observed that the central mechanism initially starts moving with motor 1, aided by the torque from the Coulomb friction of motor 2. However, after a short period, the motion halts as the power of motor 1 diminishes, causing the mechanism to enter a dead zone where its speed drops to zero. Once the motor power is increased again, the central mechanism exits the dead zone and resumes its motion.

Fig. 5-a illustrates the trajectory of the central mechanism's motion along with the applied voltages in Scenario 1. It can be observed that, despite the various states of the motors and the occurrence of multiple stick-slip phenomena, the mechanism has been able to exhibit continuous motion with relatively smooth velocity, owing to the harmonic nature of the voltage inputs. Additionally, it's noticeable that the voltage inputs in the $v_1 v_2$ plane is situated within an elliptical region. Fig. 5-b displays the voltages applied to each of the motors over time, along with mapped deadzone boundaries. These deadzone intervals can be determined based on the existing deadzones on the motor output torque and using inverse relationships of the DC motors. It can be observed that motor 1 initially resided within the deadzone with a slight deviation at the start of each sinusoidal wave but then managed to exit the deadzone, facilitating the motion of the central mechanism. Motor 2, on the other hand, remained outside the deadzone for most of the time since it was in a slipping state. Furthermore, Fig. 5-b allows us to visualize the torque transmitted from the motors to the belts. In instances where the motor was in a rolling state, the motor drive torque was transferred to the belt. However, when the motor was in a slipping state, the torque

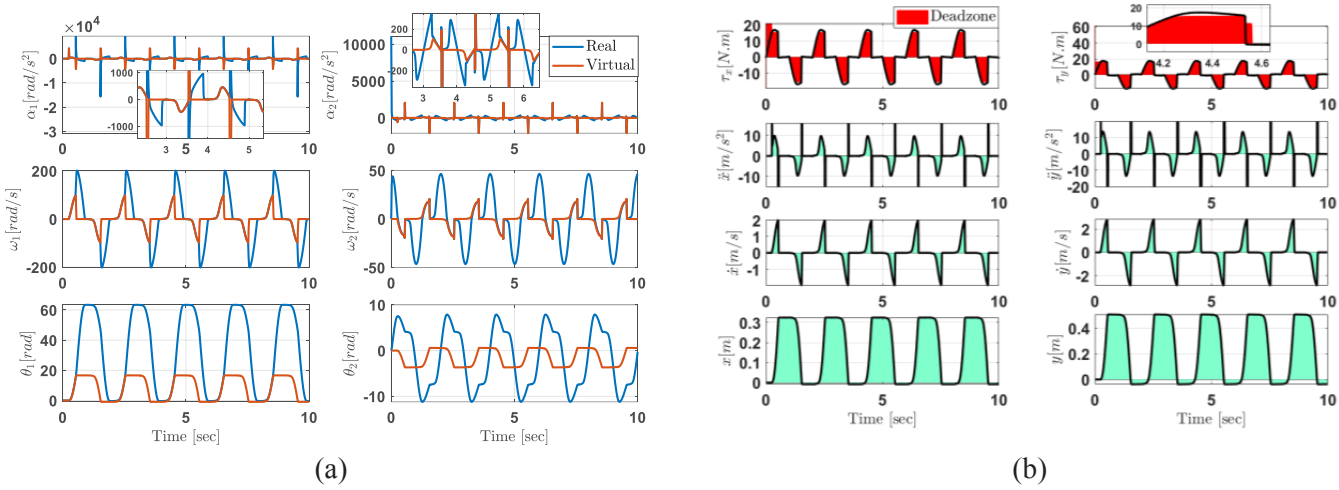

(a) (b)

Fig. 4. Simulation Results of the CoreXY Mechanism in Scenario 1. (a) Angular acceleration, angular velocity, and the angle of the actuator motors along with the corresponding values for virtual pulleys. (b) Calculated torques in the mechanism's DOF, including the deadzone intervals resulting from the friction of the mechanism's components with the ground, acceleration, velocity, and position in the DOF due to the applied torques over time

resulting from kinetic friction between the pulley and the belt was applied to the belt. Thus, it is evident that motor 1, when in a slipping state, transferred a significantly smaller amount of torque due to kinetic friction to the belt. Similarly, motor 2 was also in a slipping state, and the only torque applied to the belt was from kinetic friction. A comparison of the torque graphs transferred to the belts reveals that the magnitude of the transferred torque in the rolling state is much greater than when the motor is in a slipping state.

As seen in Fig. 6, the dynamic states of the entire system are plotted over time. In this diagram, 1 represents the RR state, 2 represents the SR state, 3 represents the RS state, and 4 represents the SS state. It can be observed that in most points, the system is in state 3 or 4, in both of which, motor 2 is in a slipping state. However, in state 3, motor 1 is in a rolling state and rotates in sync with the belt. In the remaining points, it can be seen that states 1 and 2 have occurred, each happening at a different moment.

Scenario 2:

In this scenario, simulation is performed using harmonic voltage inputs with different voltage ranges compared to Scenario 1. As shown in Table 2, in addition to increasing the voltage range of the motors, the tension forces have also been considered to be larger. To increase the likelihood of motor slips, the friction coefficients between the motor pulleys and the belts are much smaller than in Scenario 1.

Fig. 7 presents the acceleration, velocity, and position values for the motors, alongside the motion variables of the central mechanism. In Fig. 7-a, the angular acceleration, angular velocity, and angle of each motor, as well as the corresponding values for the virtual pulleys, are plotted over time. In this scenario, it can be observed that as harmonic voltage inputs are applied to the motors, they immediately begin slipping. This causes the velocities of the motor pulleys and the virtual pulleys to diverge. Fig. 7-b shows that torque values along the x-axis remain within the dead zone throughout the motion. Along the y-axis, however, the central mechanism manages to move out of the dead zone in certain intervals, resulting in minimal movement in the y-direction on the millimeter scale. A closer look at the graphs for motion in the y-direction reveals that the motion is driven by impulsive acceleration that occurs sporadically outside the dead zone. This indicates that both motors 1 and 2 were mainly in a slipping state during most of the motion. Moreover, it is evident that when the velocities of both motors drop to zero, the stick-slip phenomenon arises for the motor pulleys. This phenomenon, caused by the friction between the motor pulleys and the ground, leads to small residual velocities. When the driving torque of the motors exits the dead zone, the motors begin to move again.

As shown in Fig. 8-a, the trajectories of the central mechanism for position, velocity, and acceleration in DOF, along with the voltage inputs on the v_1 v_2 plane, are plotted.

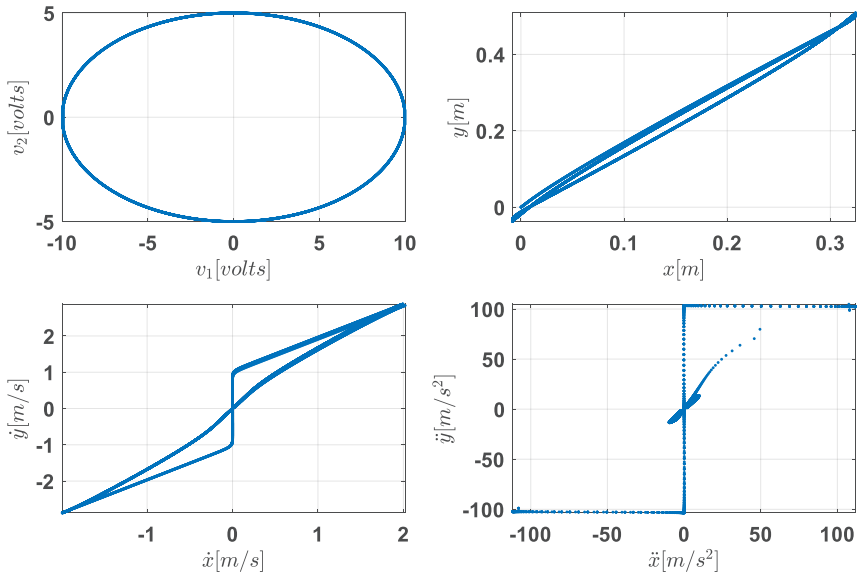

(a)

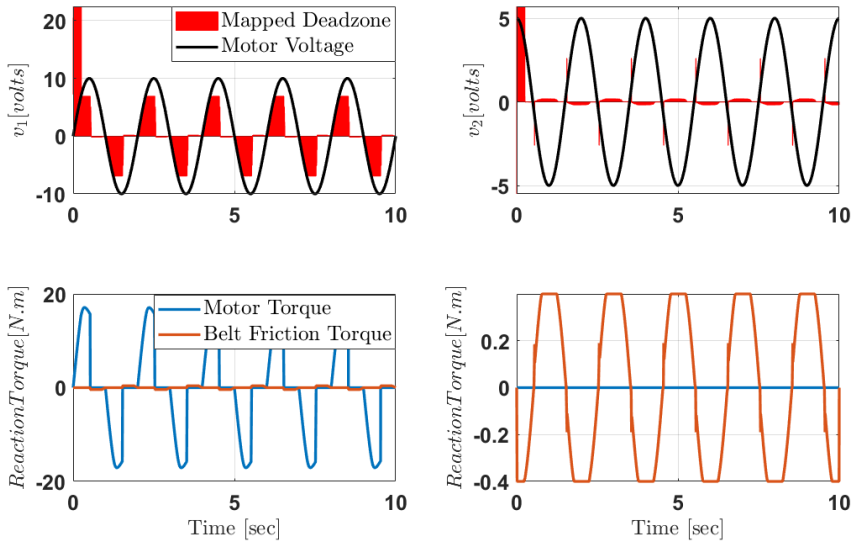

(b)

Fig. 5. Simulation results for the CoreXY mechanism in Scenario 1. (a) Trajectories of the CoreXY mechanism's DOF, including position, velocity, and acceleration in the xy planes, along with the generated voltage inputs on v_1 v_2. (b) Applied voltage inputs to the system's actuator motors over time, along with mapped deadzones on the voltages, the torques transmitted to the belts due to contact with the motor pulleys, which are in the form of motor drive torque or torque from kinetic friction

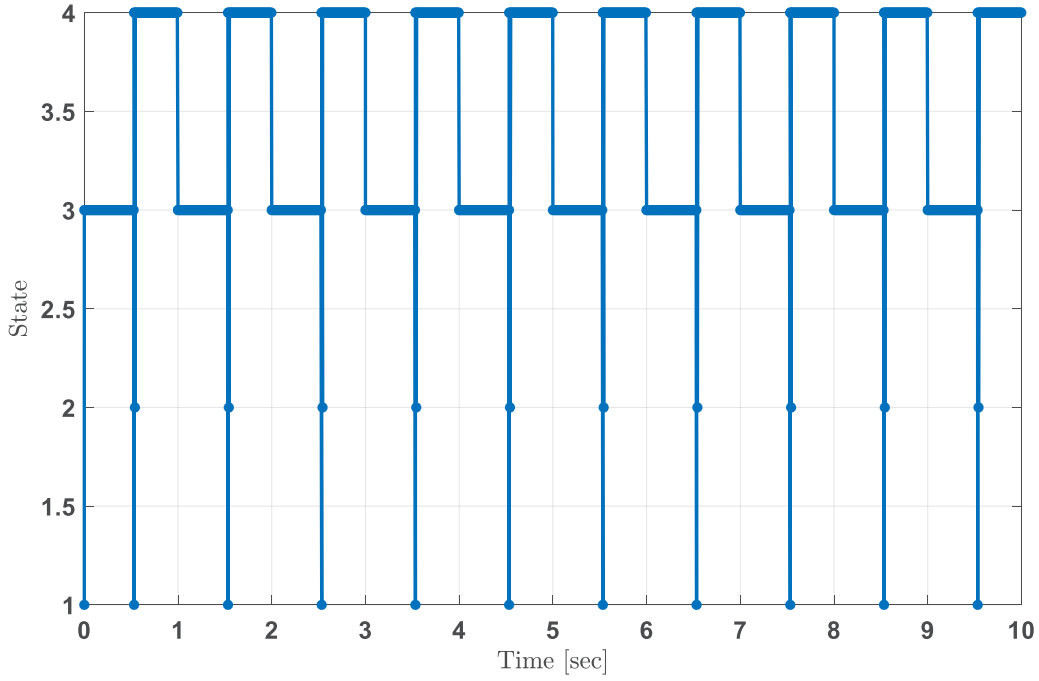

Fig. 6. State-switching dynamic model diagram of the CoreXY mechanism in Scenario 1, where 1 represents the RR state, 2 represents the SR state, 3 represents the RS state, and 4 represents the SS state

The trajectories clearly show that by applying voltage inputs in the shape of an ellipse, the central mechanism can only move in the y-direction and remains within the deadzone in the x-direction at all times. Fig. 8-b illustrates the voltage inputs applied to the motors over time, along with the mapped deadzone boundaries. It can be observed that in some instances, the voltages are within the deadzone. Nevertheless, despite experiencing stick-slip, the motors have managed to overcome disturbances caused by belt contact and continue their oscillatory motion. Additionally, in Fig. 8-b, the transferred torque values to the belts are consistently due to motion-induced friction. This indicates that both motors are in a state of slipping almost all the time. However as seen in Fig. 7-b, these torque values resulting from motion-induced friction have managed to set the central mechanism in motion in the y-direction, as evident from the trajectories.

Finally, one can observe the rolling/slipping states during the application of voltage inputs in the second scenario in Fig. 9. In almost all points, except for a few isolated instances, the system is in state 4, which is SS, meaning both motors are in a slipping state. Therefore, it can be concluded that by selecting small coefficients for the friction between the motors and the belts, the conditions for slipping both motors have been created.

Scenario 3:

In this scenario, the voltage inputs to the system will be applied in a piece-wise stepwise manner. To generate this type of input, voltages can be considered as $v_1 = \text{sign}\left[\sin\left(2\pi\omega_v t\right)\right]$, $v_2 = \text{sign}\left[\cos\left(2\pi\omega_v t\right)\right]$. This input will be applied to the motors in the form of pulses, increasing the likelihood of slipping them. Therefore, in this scenario, both coefficients of friction between the motors and the belts have been set to high values.

The simulation results of the CoreXY system, including both the mechanical motion variables and motor behavior, are presented in Fig. 10. As shown in Fig. 10-a, the angular acceleration, angular velocity, and angular position of both motors are plotted over time. Initially, both motors are in a rolling state, with their kinematic behavior matching that of the virtual pulleys. However, after about 2 seconds, both motors shift into a slipping state. Following this transition, the virtual pulleys remain stationary, indicating that the central mechanism has become immobilized. It is important to note that the frictional torque generated from dry frictional contacts was insufficient to overcome the immobilization of the central mechanism, causing it to stay within the dead zone. Moreover, Fig. 10-b shows the trajectories of acceleration, velocity, and position for the central mechanism's degrees

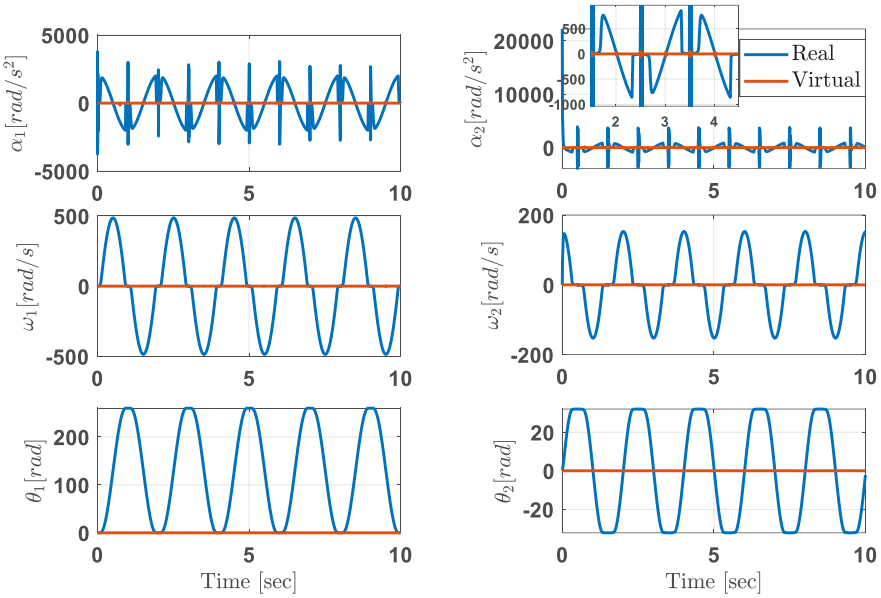

(a)

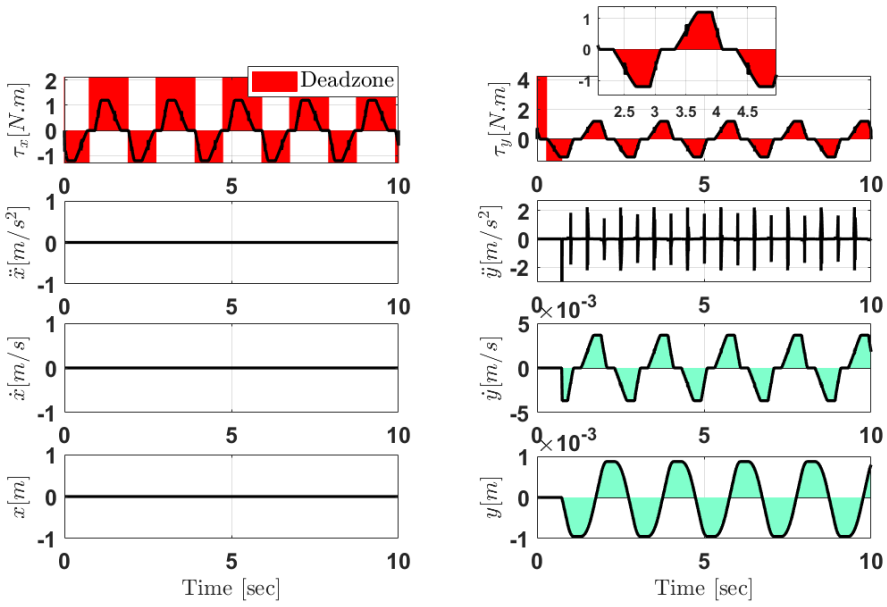

(b)

Fig. 7. Simulation results of the CoreXY mechanism in Scenario 2. (a) Angular acceleration, angular velocity, and motor angles, along with the corresponding virtual pulley values. (b) Calculated torques in the DOF of the central mechanism, along with the deadzone boundaries resulting from friction with the ground, acceleration, velocity, and position in the DOF of the central mechanism due to applied torques over time

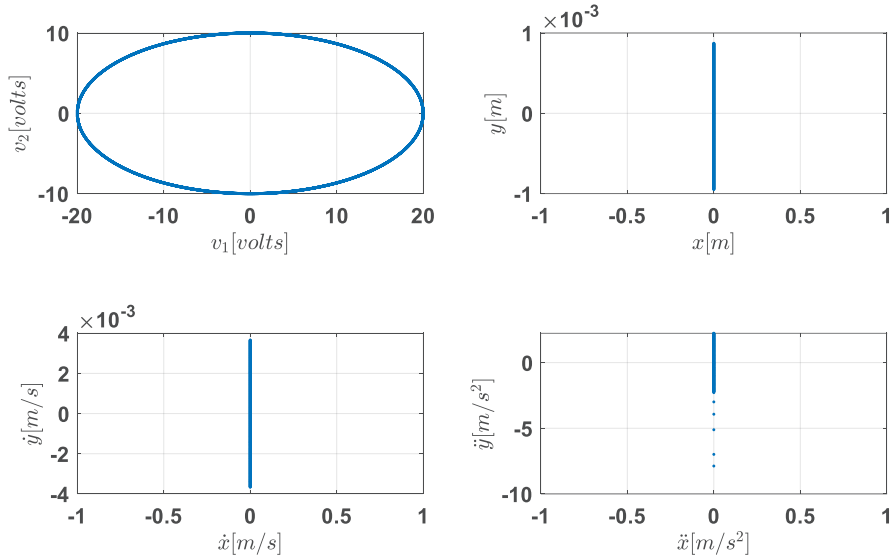

(a)

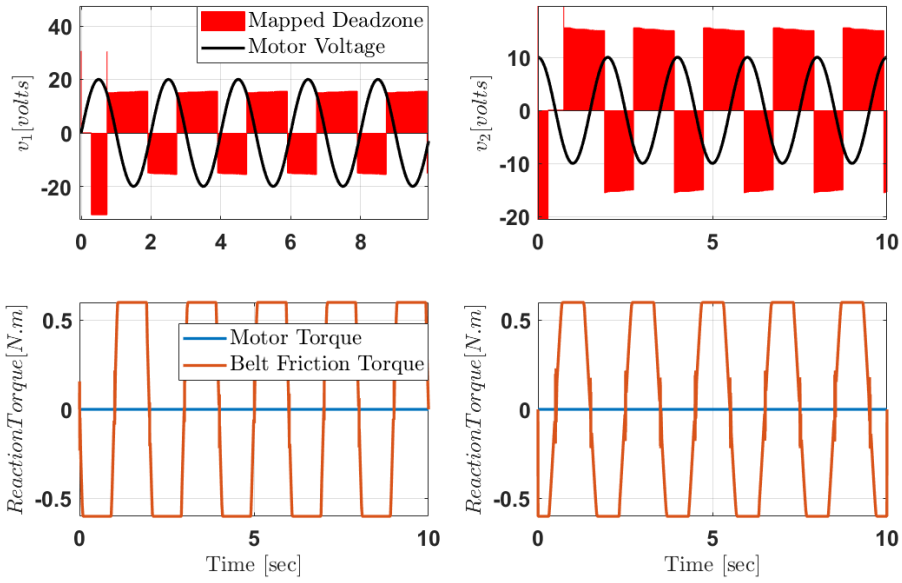

(b)

Fig. 8. Simulation results of the CoreXY mechanism in Scenario 2. (a) Trajectories of the CoreXY mechanism's DOF, including position, velocity, and acceleration in the xy planes, along with the generated voltage inputs represented on the v_1 v_2 plane. (b) Voltage inputs applied to the actuator motors over time, along with mapped deadzone boundaries on the voltages, and the transferred torques to the belts due to contact with the motor pulleys, which consist of motor driving torque and friction-induced motion torque

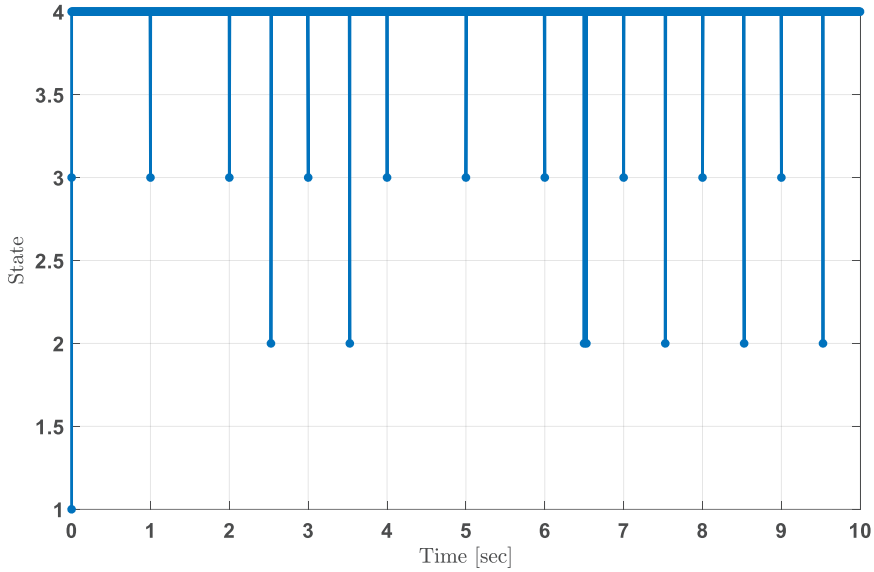

Fig. 9. The switching model dynamics plot for the CoreXY mechanism in the second scenario, where 1 represents the RR state, 2 represents the SR state, 3 represents the RS state, and 4 represents the SS state

of freedom, along with the torques applied in each direction over time. These plots reveal that after the 2-second mark, the velocity in both directions drops to zero. While some points show torques that briefly escape the dead zone, generating non-zero acceleration, the central mechanism remains in a static state.

Fig. 11-a includes the trajectories of the central mechanism in the xy plane and the voltage inputs represented in the v_1v_2 plane. It is observed that by applying voltage inputs in a piece-wise step manner, the mechanism was able to exhibit motion, which, as per Fig. 10, came to a halt after 2 seconds. Fig. 11-b illustrates the voltage inputs applied to the motors, along with the torques transferred to the belts from the motor pulleys. It is noticeable that during the initial 2 seconds of motion, the voltage inputs exceeded the mapped deadzone boundaries and were able to set the mechanism in motion. However, after that, the motors experienced slipping. Furthermore, in Fig. 11-b, it can be observed that during the initial 2 seconds when both motors were in the rolling state, the torques transferred to the belts were essentially the motor drive torques. Yet, with the slipping of the motor pulleys, the torques transferred to the belts due to frictional interaction were calculated. These torques have a significantly smaller range than before and were unable to put the central mechanism into motion.

As observed in the results of the third scenario, both motors were initially in the RR state, but due to the resistant torques resulting from inertia and the accelerations of the central mechanism, they started slipping and transitioned to the SS state. This transition is clearly depicted in Fig. 12.

4- Conclusion

In this paper, the modeling and dynamic analysis of the CoreXY mechanism, which includes the possibility of motor pulley slipping, were investigated. The work began with extracting the kinematic relationships of the system components and defining virtual pulleys. After determining the static and kinetic frictions for each of the system components, various rolling/slipping states of the system were examined. In the equations of motion for the central mechanism, which includes all components except the motor pulleys, it was observed that due to the friction between the actuator components and the ground, the system is susceptible to the nonlinear phenomenon of stick-slip, leading to the creation of deadzones in the actuator system during motion initiation. Therefore, a new friction model was introduced, including the deadzone, and the equations accounting for the stick-slip phenomenon were derived. Additionally, considering that each of the actuator motors can be in a rolling or slipping state, it was determined that the CoreXY mechanism is, in fact, a hybrid-DOF dynamic system. Its equations switch among four modes: RR, SR, RS, and SS. The specific mode the system adopts depends on the input voltages of each motor, kinematic and dynamic variables at the current time, as well as the friction coefficients between the motor pulleys

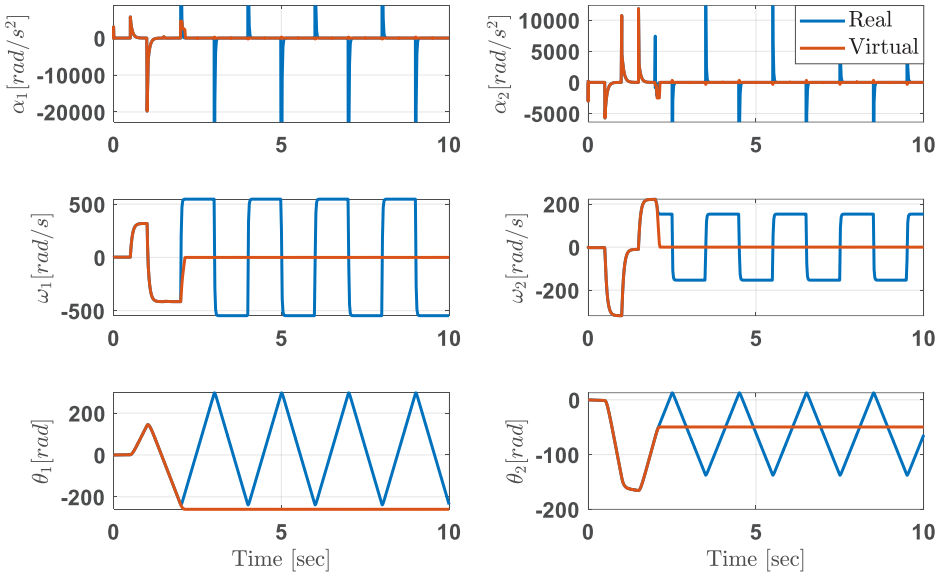

(a)

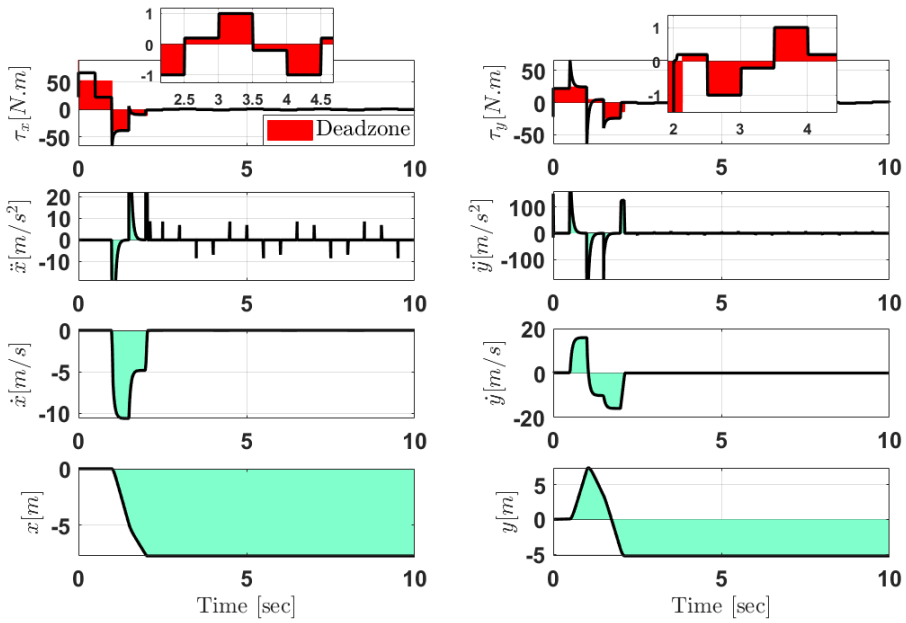

(b)

Fig. 10. Simulation results of the CoreXY mechanism in Scenario 3. (a) Angular acceleration, angular velocity, and motor angles with corresponding virtual pulley values. (b) Computed torques in the DOF of the central mechanism along with the deadzone intervals resulting from the friction between mechanical components and the ground, acceleration, velocity, and position in the DOF of the central mechanism due to the application of torques over time

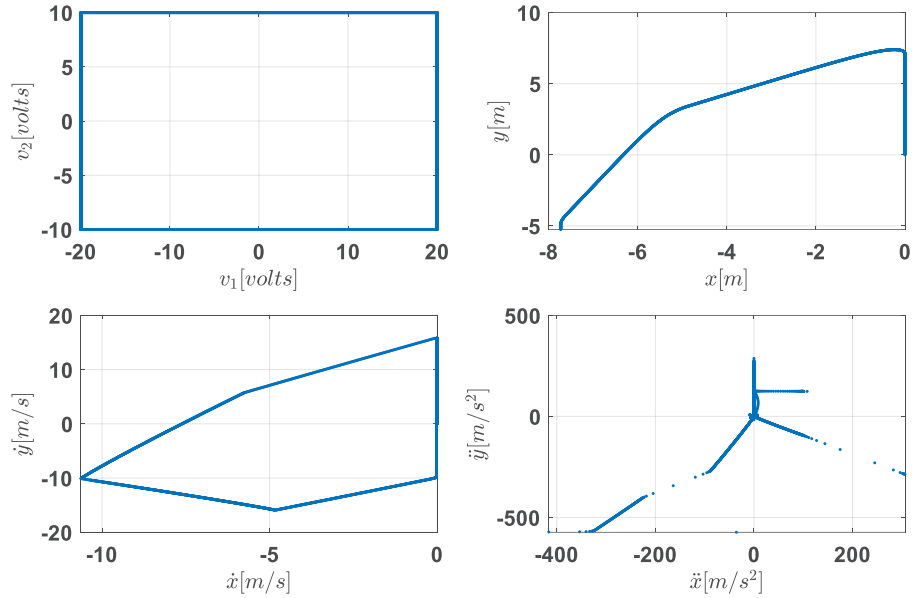

(a)

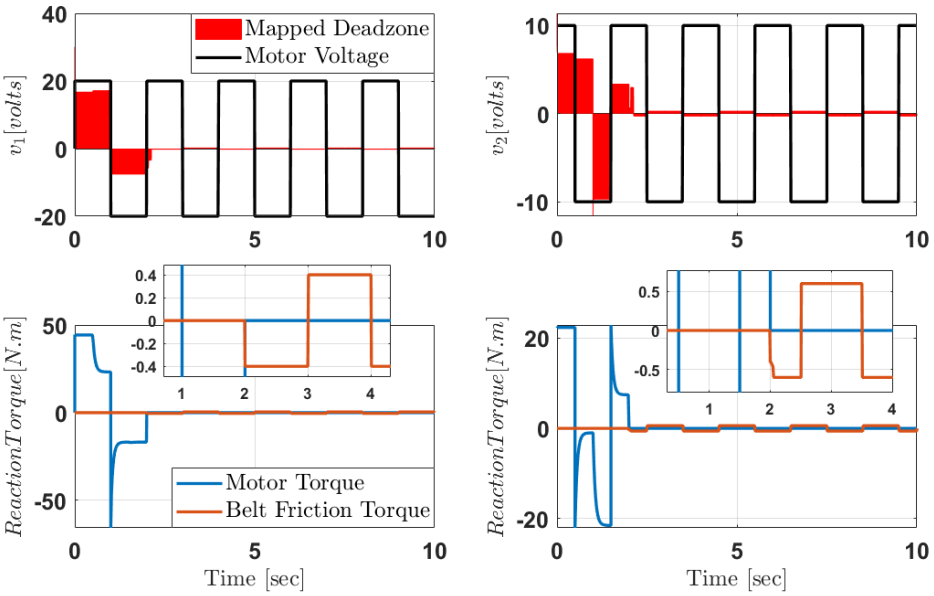

(b)

Fig. 11. Simulation Results of the CoreXY Mechanism in Scenario Three. (a) Trajectories of the DOF of the CoreXY mechanism, including position, velocity, and acceleration in the xy planes, along with the generated voltage inputs represented in the v_1 v_2 plane. (b) Voltage inputs applied to the operative motors of the system over time, along with the mapped deadzone boundaries on the voltage inputs, and the transferred torques to the belts due to interactions with the motor pulleys, either in the form of motor drive torque or frictional torque

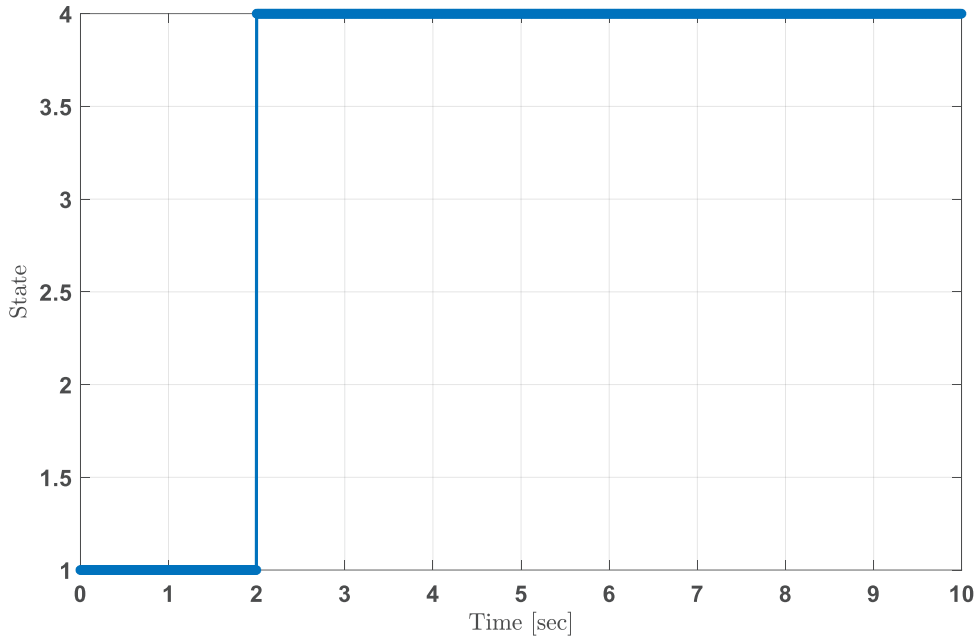

Fig. 12. The switch model dynamic diagram of the CoreXY mechanism in the third scenario, where 1 represents the RR state, 2 represents the SR state, 3 represents the RS state, and 4 represents the SS state.

and the belts. Thus, it is necessary to calculate the required friction to keep a motor in the rolling state. If the existing friction between the motor pulley and the belt is insufficient, the motor slips. This determination for the next step of the system's dynamics was performed as a combination of different states of the two motors, taking into account the change in the system's DOF in each state and the presence of the stick-slip phenomenon along with the deadzone. Finally, dynamic analysis of the CoreXY mechanism in various scenarios was conducted by simulating the derived equations in three different scenarios, effectively illuminating all the nonlinear effects and complexities of this mechanism. In summary, the results obtained from the mentioned scenarios are as below.

- Scenario 1 (Harmonic Voltage Inputs and Slip Dynamics): Motor 1 was rolling, but Motor 2 slipped immediately. Increasing the voltage led motor 1 to also begin slipping. The central mechanism started moving due to motor 1 and the Coulomb friction torque of motor 2 but stopped shortly after motor 1's power was reduced, entering a dead zone with zero velocity. Despite multiple stick-slip events, the mechanism exhibited continuous and relatively smooth motion, thanks to the harmonic voltage inputs.
- Scenario 2 (Harmonic Voltage Inputs with Varying Range): With the harmonic voltage inputs, both motors slipped immediately, leading to differing velocities between the motor pulley and the virtual pulley. Occasional exits from the dead zone along the y-axis resulted in small, millimeter-scale movements due to impulsive accelerations. Transferred torques to the belts were primarily due to motion-induced friction, which drove the central mechanism in the y-direction. Motors remained in a slipping state most of the time.
- Scenario 3 (Piece-wise Inputs): Initially, both motors were in a rolling state with their kinematic behavior matching the virtual pulleys. After about 2 seconds, both motors transitioned to slipping. Following the motor slip, the virtual pulleys remained stationary, immobilizing the central mechanism. The frictional torque from dry contacts was insufficient to restart the motion, keeping the mechanism in the dead zone. Both motors began in a rolling state (RR), but inertia and acceleration forces led to slipping, transitioning the motors into a slipping state (SS).

Future Works

This team, considering the findings of this paper, has so far addressed the modeling of the CoreXY mechanism, taking into account the stick-slip phenomenon along with the deadzone and the presence of various rolling/slipping states for the system's motors. This has led to the development of a hybrid-DOF dynamic model. In future work, further nonlinear effects of the CoreXY mechanism, such as the impact of belt tension and weight, could be incorporated into the modeling. Furthermore, with the formulation of the equations for this mechanism as a hybrid-DOF dynamic model, the

control of such a system with two control inputs will present substantial challenges that need to be addressed.

Conflict of Interest Statement:

This study includes no potential conflict of interest.

Data Availability Statement:

This study includes no used data.

References

[1] M. Moeen and M. Reza, "Numerical algorithm for nonlinearity compensation of hardly constrained actuation for trajectory tracking control of deadzone-included dynamic systems," ISA Trans., no. xxxx, 2024, doi: 10.1016/j.isatra.2024.07.025.

[2] M. Ebrahimi and M. Homaeinezhad, "Compensation of friction and stick-slip uncertainties in trajectory tracking control of servo DC machines considering actuation constraints," https://doi.org/10.1177/09596518231196830, Oct. 2023, doi: 10.1177/09596518231196830.

[3] M. Lahoud, G. Marchello, M. D'Imperio, A. Müller, and F. Cannella, "A Deep Learning Framework for Non-Symmetrical Coulomb Friction Identification of Robotic Manipulators," Proc. - IEEE Int. Conf. Robot. Autom., pp. 10510–10516, 2024, doi: 10.1109/ICRA57147.2024.10610737.

[4] S. Mahajan and A. Cicirello, "Governing Equation Identification of Nonlinear Single Degree-of-Freedom Oscillators With Coulomb Friction Using Explicit Stick and Slip Temporal Constraints," ASCE-ASME J. Risk Uncertain. Eng. Syst. Part B Mech. Eng., vol. 9, no. 4, Dec. 2023, doi: 10.1115/1.4063070/1166116.

[5] A. Amthor, S. Zschaeck, and C. Ament, "High precision position control using an adaptive friction compensation approach," IEEE Trans. Automat. Contr., vol. 55, no. 1, pp. 274–278, 2010, doi: 10.1109/TAC.2009.2036307.

[6] A. Shahhosseini, M. H. Tien, and K. D'Souza, "Efficient Hybrid Symbolic-Numeric Computational Method for Piecewise Linear Systems With Coulomb Friction," J. Comput. Nonlinear Dyn., vol. 18, no. 7, Jul. 2023, doi: 10.1115/1.4062203/1160344.

[7] J. Shah, B. Snider, T. Clarke, S. Kozutsky, M. Lacki, and A. Hosseini, "Large-scale 3D printers for additive manufacturing: design considerations and challenges," Int. J. Adv. Manuf. Technol., vol. 104, no. 9–12, pp. 3679–3693, 2019, doi: 10.1007/s00170-019-04074-6.

[8] J. O. Jang, "Deadzone compensation of an XY-positioning table using fuzzy logic," IEEE Trans. Ind. Electron., vol. 52, no. 6, pp. 1696–1701, 2005, doi: 10.1109/TIE.2005.858702.

[9] Z. Zhao et al., "Adaptive Quantized Control of Flexible Manipulators Subject to Unknown Dead Zones," IEEE Trans. Syst. Man, Cybern. Syst., vol. 53, no. 10, pp. 6438–6447, Oct. 2023, doi: 10.1109/TSMC.2023.3283268.

[10] K. S. Sollmann, M. K. Jouaneh, and D. Lavender, "Dynamic modeling of a two-axis, parallel, H-frame-type XY positioning system," IEEE/ASME Trans. Mechatronics, vol. 15, no. 2, pp. 280–290, 2010, doi: 10.1109/TMECH.2009.2020823.

[11] S. He, H. Tang, Z. Zhu, P. Zhang, Y. Xu, and X. Chen, "A novel flexure piezomotor with minimized backward and nonlinear motion effect," IEEE Trans. Ind. Electron., vol. 69, no. 1, pp. 652–662, 2022, doi: 10.1109/TIE.2020.3048320.

[12] L. Yuan, L. Wang, R. Qi, Z. Zhao, J. Jin, and C. Zhao, "A novel hollow-type XY piezoelectric positioning platform," Int. J. Mech. Sci., vol. 255, p. 108496, Oct. 2023, doi: 10.1016/J.IJMECSCI.2023.108496.

[13] M. Miyasaka, M. Haghighipanah, Y. Li, J. Matheson, A. Lewis, and B. Hannaford, "Modeling Cable-Driven Robot with Hysteresis and Cable-Pulley Network Friction," IEEE/ASME Trans. Mechatronics, vol. 25, no. 2, pp. 1095–1104, 2020, doi: 10.1109/TMECH.2020.2973428.

[14] M. R. Homaeinezhad and M. M. Ebrahimi, "Numerical Approach for Nonlinear Dynamics Simulation of Belt-Pulley XY Positioning Mechanism," pp. 352–373, 2024, doi: 10.37256/est.5220244538.

[15] M. R. Homaeinezhad, M. Homaeinezhad, S. Akbari, and D. Nayeb Ghanbar Hosseini, "Input-decoupled discrete-time sliding mode control algorithm for servo multi-field multi-armature DC machine," ISA Trans., vol. 127, no. xxxx, pp. 283–298, 2022, doi: 10.1016/j.isatra.2021.08.037.

[16] A. Izadbakhsh, N. Nassiri, and M. B. Menhaj, "Linear/Nonlinear PID Control of Cooperative Multiple Robot Manipulators: A Robust Approach," AUT J. Model. Simul., vol. 55, no. 1, pp. 5–5, Jun. 2023, doi: 10.22060/MISCJ.2023.21867.5305.

[17] E. Ostertag, N. Bakri, and N. Becker, "Functional Disturbance Observer for Simultaneous Control and Dry Friction Compensation," IFAC Proc. Vol., vol. 22, no. 6, pp. 421–426, 1989, doi: 10.1016/s1474-6670(17)54412-2.

[18] H. Ahmadian, I. Sharifi, and H. A. Talebi, "Robust Distributed Lasso-Model Predictive Control Design: A Case Study on Large-Scale Multi-Robot Systems," AUT J. Model. Simul., vol. 55, no. 1, pp. 8–8, Jun. 2023, doi: 10.22060/MISCJ.2023.22087.5312.

[19] E. Jahanbazi, F. Jahangiri, and M. R. Mohammadi, "Neural Network based Fault Tolerant LQR Control for Orbital Maneuvering in LEO Satellites using Hall Effect Thrusters," AUT J. Model. Simul., vol. 55, no. 1, pp. 11–11, Jun. 2023, doi: 10.22060/MISCJ.2023.22482.5326.

[20] W. W. Yao, X. P. Zhou, D. Dias, Y. Jia, and Y. J. Li, "Frictional contact and stick-slip: Mechanism and numerical technology," Int. J. Solids Struct., vol. 274, p. 112289, Jul. 2023, doi: 10.1016/J.IJSOLSTR.2023.112289.

[21] B. Shi, F. Wang, C. Han, Z. Huo, and Y. Tian, "Design of a precise positioning stage actuated by a double-layer

stick-slip actuator used for precise assembly," Mech. Mach. Theory, vol. 185, p. 105336, Jul. 2023, doi: 10.1016/J.MECHMACHTHEORY.2023.105336.

[22] G. S. Mfoumou, G. D. Kenmoé, and T. C. Kofané, "Computational algorithms of time series for stick-slip dynamics and time-delayed feedback control of chaos for a class of discontinuous friction systems," Mech. Syst. Signal Process., vol. 119, pp. 399–419, 2019, doi: 10.1016/j.ymssp.2018.09.034.

[23] G. Qiao, H. Li, X. Lu, J. Wen, and T. Cheng, "Piezoelectric stick-slip actuators with flexure hinge mechanisms: A review," https://doi.org/10.1177/1045389X211072244, vol. 33, no. 15, pp. 1879–1901, Jan. 2022, doi: 10.1177/1045389X211072244.

[24] W. Liu, F. Yang, X. Zhu, and X. Chen, "Stick-slip vibration behaviors of BHA and its control method in highly-deviated wells," Alexandria Eng. J., vol. 61, no. 12, pp. 9757–9767, 2022, doi: 10.1016/j.aej.2022.01.039.

[25] Y. Lu et al., "Experimental investigation of stick-slip behaviors in dry sliding friction," Tribol. Int., vol. 201, p. 110221, Jan. 2025, doi: 10.1016/J.TRIBOINT.2024.110221.

[26] Q. Huang, Z. Xie, and H. Liu, "Active control for stick-slip behavior of the marine propeller shaft subjected to friction-induced vibration," Ocean Eng., vol. 268, no. September 2022, p. 113302, 2023, doi: 10.1016/j.oceaneng.2022.113302.

[27] M. R. Homaeinezhad, M. M. Ebrahimi, and M. M. M. Alvar, "Discrete-Time Nonlinear Control Technique for Trajectory Tracking of Hybrid Reluctance Actuator," pp. 1–27, 1999, doi: 10.24200/sci.2024.63806.8606.

[28] D. Zhang, L. Kong, S. Zhang, Q. Li, and Q. Fu, "Neural networks-based fixed-time control for a robot with uncertainties and input deadzone," Neurocomputing, vol. 390, pp. 139–147, 2020, doi: 10.1016/j.neucom.2020.01.072.

[29] G. Galuppini, L. Magni, and D. Martino, "Model predictive control of systems with deadzone and saturation Model Predictive Control of Systems with Deadzone and Saturation," no. February 2023, 2018, doi: 10.1016/j.conengprac.2018.06.010.

HOW TO CITE THIS ARTICLE

M. M. Ebrahimi, M. R. Homaeinezhad, Numerical Algorithm for Simulation of Hybrid-Degrees of Freedom Belt-Pulley Systems: Application to X-Y Positioning Mechanism, AUT J. Model. Simul., 56(2) (2024) 129-154.

DOI: 10.22060/miscj.2024.22932.5350